CMS Physics Analysis Summary

Contact: cms-pag-conveners-susy@cern.ch 2015/12/15

Search for supersymmetry in pp collisions at $\sqrt{s} = 13$ TeV in the single-lepton final state using the sum of masses of large radius jets

The CMS Collaboration

Abstract

Results are reported from a search for supersymmetric particles in pp collisions in the final state with a single, high p_{T} lepton; multiple jets, including at least one b-tagged jet; and large missing transverse momentum. The data sample corresponds to 2.1 fb^{-1} recorded by the CMS experiment at $\sqrt{s} = 13$ TeV. The search focuses on processes leading to high jet multiplicities, such as $\mathrm{gg} \to \tilde{\mathrm{g}}\tilde{\mathrm{g}}$ with $\tilde{\mathrm{g}} \to \mathrm{t\bar{t}}\,\tilde{\chi}_1^0$. The quantity M_J, defined as the sum of the masses of the large-radius jets in the event, is used in conjunction with other kinematic variables to provide discrimination between signal and backgrounds and as a key part of the background estimation method. The observed event yields in the signal regions in data are consistent with those expected for standard model backgrounds, which are estimated from control regions. Exclusion limits are obtained for the simplified model T1tttt, which corresponds to gluino pair production with decays into top quarks plus neutralinos. Gluinos with mass below 1575 GeV are excluded at 95% CL for T1tttt scenarios with low $\tilde{\chi}_1^0$ mass.

1 Introduction

This document presents the results from a search for supersymmetry (SUSY) [1–8] in the final state with a single isolated lepton; multiple jets, including at least one b-tagged jet; and large missing transverse momentum. The search targets gluino pair production with $\tilde{g} \to t\bar{t}\tilde{\chi}_1^0$, which arises from $\tilde{g} \to \tilde{t}\bar{t}$, where the top-squark is produced off mass shell. This scenario is shown in Fig. 1 and is designated T1tttt in simplified model scenarios [9–11]. A total of four top quarks are produced in the final state, which typically contains a large number of jets, four of which are b jets from top-quark decay. Depending on the decay modes of the accompanying W-bosons, a range of lepton multiplicities is possible; we focus here on the single-lepton final state.

Signatures of this type are particularly relevant in the context of so-called natural SUSY models [12–14], which are motivated by the gauge hierarchy problem. In the standard model, the presence of quantum corrections to Higgs-boson mass, in the absence of extreme fine tuning, destabilizes the electroweak mass scale, pulling it to the cutoff scale of the theory. SUSY models with relatively light top and bottom squarks ($\tilde{t}_L$, $\tilde{t}_R$, $\tilde{b}_L$), gluinos ($\tilde{g}$), and Higgsinos ($\tilde{h}$) can maintain the low observed value of the electroweak scale.

In this analysis, the scalar sum of the masses of large-R jet masses,

$$M_J = \sum_{J_i = \text{large}-R \text{ jets}} m(J_i), \tag{1}$$

is used both to characterize the hadronic activity in the event, providing discrimination between signal and background, and as a key part of a robust methodology for background estimation. A key property of M_J exploited in this analysis is that its distribution for the dominant background, $t\bar{t}$ production, is nearly uncorrelated with that of the variable m_T, the transverse mass of the lepton + $\vec{p}_T^{\,\text{miss}}$ system. The missing momentum vector, $\vec{p}_T^{\,\text{miss}}$, is defined in the plane transverse to the direction of the colliding proton beams; its magnitude is denoted E_T^{miss}. The absence of correlation between M_J and m_T allows one to measure the background shape using a control sample at low m_T and applying it to the high m_T sample, which includes the signal region. The quantity M_J was first discussed in phenomenological studies, for example, Refs. [15–17]. We have presented studies of M_J using early 13 TeV data [18].

This document is organized as follows. Section 2 discusses the data and simulated event samples used in the analysis. The reconstruction objects, including leptons, jets, and large-R jets, are discussed in Section 3. The variable M_J is shown to provide discrimination between signal and the $t\bar{t}$ background. Its distribution, and particularly its tail, are sensitive to initial-state radiation (ISR), which plays a key role in the analysis because of the high jet-multiplicity requirements used to suppress $t\bar{t}$ events. The trigger and event selection are presented in Sec-

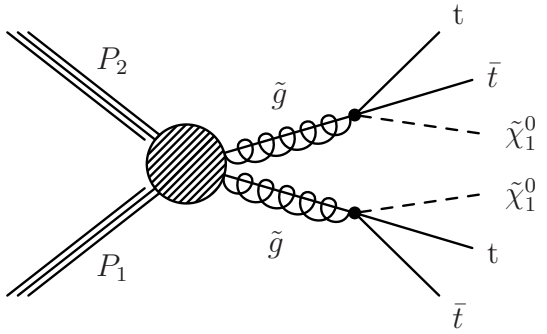

Figure 1: Gluino pair production and decay for the simplified model T1tttt.

tion 4. The different sources of background are detailed, and it is shown that the dominant background arises from a single source, dilepton $\mathrm{t\bar{t}}$ events. A basic description of the analysis binning is also presented. Section 5 describes the methodology of the background estimation, which depends on kinematic properties of M_J. A key feature of the analysis is the relationship between M_J for single-lepton $\mathrm{t\bar{t}}$ and dilepton $\mathrm{t\bar{t}}$ events and how this is affected by ISR. The maximum likelihood fit procedures used for the signal extraction are also described. Section 6 discusses the systematic uncertainties on the background estimate and the signal efficiency. The observed event yields in data are presented in Section 7; these are compared with background predictions and used to obtain exclusion limits for the T1tttt simplified model. Finally, Section 8 presents a summary of the methodology and the results.

2 Event samples

The analysis was performed using a data sample of pp collisions at $\sqrt{s} = 13$ TeV. The sample was obtained with the CMS detector and corresponds to an integrated luminosity of 2.1 fb^{-1}.

While the background estimation in the analysis is performed largely from control samples in the data, simulated events samples are also used to provide correction factors, typically near unity, that are used to account for specific effects that could bias the background predictions. Large backgrounds are simulated with MADGRAPH5_AMC@NLO generator [19] in leading-order mode. Samples corresponding to vector bosons produced in association with jets are simulated with up to 4 additional partons from the Matrix Element, $\mathrm{t\bar{t}}$ with up to 3 and QCD with up 2 additional partons. Single top is produced at NLO with MADGRAPH5_AMC@NLO for the *s*-channel and POWHEG [20, 21] for the *t*-channel and *W*-associated production. Additional smaller backgrounds, such $\mathrm{t\bar{t}}$ in association with vector bosons and dibosons are similarly produced at NLO with either MADGRAPH5_AMC@NLO or POWHEG. The generation uses the NNPDF 3.0 [22] set of parton distribution functions. Parton showering and fragmentation are modeled with the PYTHIA8 [23] generator and the detector simulation is performed with GEANT4 [24]. The signal samples are also generated with MADGRAPH5_AMC@NLO in leading-order mode with up to 2 additional partons using the NNPDF 3.0 PDF set, but their propagation through the detector is modeled using the CMS Fast Simulation [25]. The cross sections used to scale the events use the highest order calculation available. In particular, the $\mathrm{t\bar{t}}$ background is calculated to NNLO+NNLL order [26] and the signal yields are calculated to NLO+NLL resummation [27–30]. In the case of $\mathrm{t\bar{t}}$, we also apply a top p_{T} reweighting motivated by 8TeV measurements and cross-checked in 13 TeV data, while keeping the overall normalization fixed to the NNLO+NNLL cross-section.

3 Reconstruction objects and variable definitions

Table 1 lists the main reconstruction objects and associated requirements used in the analysis. Jets are clustered with the anti-k_{T} [31] algorithm with a distance parameter of $R = 0.4$. These jets are further clustered to reconstruct large-*R* jets, which serve as inputs to calculating the M_J variable. The reconstruction and identification of isolated leptons, small-*R* (standard) jets, large-*R* jets, and b-tagged jets, as well as the properties of the M_J variable, are discussed in the sections below.

The missing transverse energy, $E_{\mathrm{T}}^{\mathrm{miss}}$, is given by the magnitude of the vector sum, $\vec{p}_{\mathrm{T}}^{\,\mathrm{miss}}$, of the transverse momenta of all the Particle Flow (PF) candidates [32, 33]. Its correspondence to the true undetectable energy in the event is improved by replacing the contribution of the PF candidates that are associated with a jet by the jet's calibrated four-momentum, referred

Table 1: Summary of object selection requirements.

Object	p_T [GeV]	$\|\eta\|$	Other
Electrons	20	2.5	$I_{\text{mini}} < 0.1$
Muons	20	2.4	$I_{\text{mini}} < 0.2$
Jets	30	2.4	Anti-k_t R=0.4, cleaned from leptons
b-tags	30	2.4	Jets with CSVv2IVF tag
MET	–	–	Type-I corrected E_T^{miss}

to as the Type-I MET correction. To separate backgrounds characterized by the presence of a single W-boson and no other source of missing energy, the lepton and the MET are combined to obtain the transverse mass, m_T defined as:

$$m_T = \sqrt{2p_T^{\ell} E_T^{\text{miss}} (1 - \cos(\phi_\ell - \phi_{E_T^{\text{miss}}}))}, \tag{2}$$

where ϕ_ℓ is the azimuthal angle of the lepton momentum vector and $\phi_{E_T^{\text{miss}}}$ is the azimuthal angle of the missing momentum vector, $\vec{p}_T^{\text{miss}}$.

3.1 Leptons

Electrons are reconstructed based on the association of a charged track and an ECAL supercluster [34]. The resulting candidates required to satisfy identification criteria designed to minimize contributions from light-jet fakes, photon conversions, and real electrons coming from heavy flavor decays. Electron candidates must satisfy $p_T > 20$ GeV and $|\eta| \leq 2.5$.

Muons are reconstructed using the outside-in approach, where each stand-alone muon track found in the muon system serves as a seed to find a corresponding silicon track [35]. Muon candidates must have $p_T > 20$ GeV and $|\eta| < 2.4$.

Lepton isolation is quantified using an optimized version of the mini-isolation variable originally suggested in Ref. [36]. Charged leptons in proton-proton collisions can be produced either in the decays of heavy particles (W or Z bosons, or heavy non-SM particles), in which case the leptons are considered to be primary or prompt, or in the decays of lighter SM particles, particularly b-hadrons, in which case the leptons are considered to be secondary or non-prompt. In this analysis, we wish to exclude secondary leptons. Since such leptons are frequently found in or near the jet produced by the decay of the associated quark, they can be rejected by requiring that only a small amount of energy be deposited in the detector near the lepton. To quantify the transverse energy near a lepton, the relative isolation I for each lepton is computed as the sum of the transverse momenta of PF candidates in a cone around the lepton, divided by the p_T of the lepton:

$$I = \frac{1}{p_T^{\text{lep}}} \Bigg\{ \sum_{\text{cone}} p_T(\text{charged hadrons from PV}) + \max \left[0, \sum_{\text{cone}} p_T(\text{phot.}) + \sum_{\text{cone}} p_T(\text{ntrl. had.}) - \frac{1}{2} \sum_{\text{cone}} p_T(\text{chg. had. not from PV}) \right] \Bigg\}. \tag{3}$$

The last term is a correction that estimates the average amount of pileup energy (which arises from the presence of multiple pp interactions in a single bunch crossing) near the leptons by taking the contribution from charged candidates not originating from the primary vertex and multiplying by $\frac{1}{2}$ to account for the average difference in neutral and charged contributions from pileup.

For the standard isolation calculation, PF candidates within a fixed radius cone in $\Delta\eta\Delta\varphi$ space are summed in Eq. (3). This is not ideal in events with highly boosted t decays, as the b and W will become closer, and the prompt lepton from the W decay may coincidentally fall within the b-jet. For a generic highly boosted two body decay, the angle between the two daughter particles is given by

$$\Delta R_{\text{daughters}} \approx \frac{2m_{\text{mother}}}{p_{T,\text{mother}}}. \tag{4}$$

Since isolation is intended to remove leptons originating from b-decays, the isolation cone size should be approximately the size of the associated b-jet. Using $m_{\text{mother}} = 5$ GeV $\approx m_{\text{b}}$ and taking the p_{T} of the lepton to be a crude proxy for the p_{T} of the b motivates the following $p_{\text{T}}^{\text{lep}}$-dependent cone size:

$$\Delta R_{\text{max}}^{\text{mini-iso.}} = \begin{cases} 0.2, & p_{\text{T}}^{\text{lep}} \leq 50 \text{ GeV} \\ \frac{10 \text{ GeV}}{p_{\text{T}}^{\text{lep}}}, & p_{\text{T}}^{\text{lep}} \in (50 \text{ GeV}, 200 \text{ GeV}) \\ 0.05, & p_{\text{T}}^{\text{lep}} \geq 200 \text{ GeV}, \end{cases} \tag{5}$$

The p_{T}-dependent cone size is small enough to reduce accidental overlap with b and other jets for prompt leptons, while remaining large enough to contain b-decay products for non-prompt leptons across a range of $p_{\text{T}}^{\text{lep}}$. We refer to the relative isolation (Eq. 3) computed with the cone size described in Eq. 5 as mini-isolation.

3.2 Small-R jets, Large-R (fat) jets, and M_J

Small-R jets are built from PF candidates using the anti-k_{T} algorithm with a radius R=0.4 [37]. Their neutral electromagnetic and hadronic energy fractions must each be less than 99%, and they are required to contain at least one neutral, charged, or muon PF candidate. For those jets falling inside the tracking region, the charged electromagnetic fraction should be less than 99%, while the charged hadronic energy fraction should be greater than zero. Contributions to an individual jet's p_{T} from pileup interactions are subtracted [38]. The jet energy is calibrated [39] following the standard sequence of corrections including: L1, a pile-up offset correction taking into account the jet's active area; L2, a relative jet energy scale derived from di-jet balance, aiming to make the jet response uniform in p_{T} and η; L3, an absolute jet energy scale derived in γ+jet events based on the MET Projection Fraction method and p_{T} balance; and a residual L2L3 correction, applied to account for any remaining data/MC disagreement.

The corrected jet must satisfy the requirements $p_{\text{T}} > 30$ GeV and $|\eta| \leq 2.4$, as well as a set of quality criteria [40]. Finally, the jet collection is cleaned by removing any jet that has a PF constituent matching a lepton passing the selection described earlier. Using the resulting jet collection, the transverse hadronic energy, H_{T}, is defined as the scalar sum of the jet transverse momenta.

Jets originating from b-quarks are identified by the Combined Secondary Vertex algorithm [41] together with the Inclusive Vertex Finder (IVF). The CSV algorithm uses both secondary vertex and track-based information, thereby maximizing the highest attainable efficiency while providing discrimination even in cases where only 2-track pseudo-vertices or no secondary vertex is reconstructed. The IVF provides track-to-jet association such that tracks and secondary vertices are not shared between nearby jets, improving the b-tagging performance in boosted topologies. We use a working point with 70% b-tagging efficiency and 1.5% light-jet misidentification rate [42].

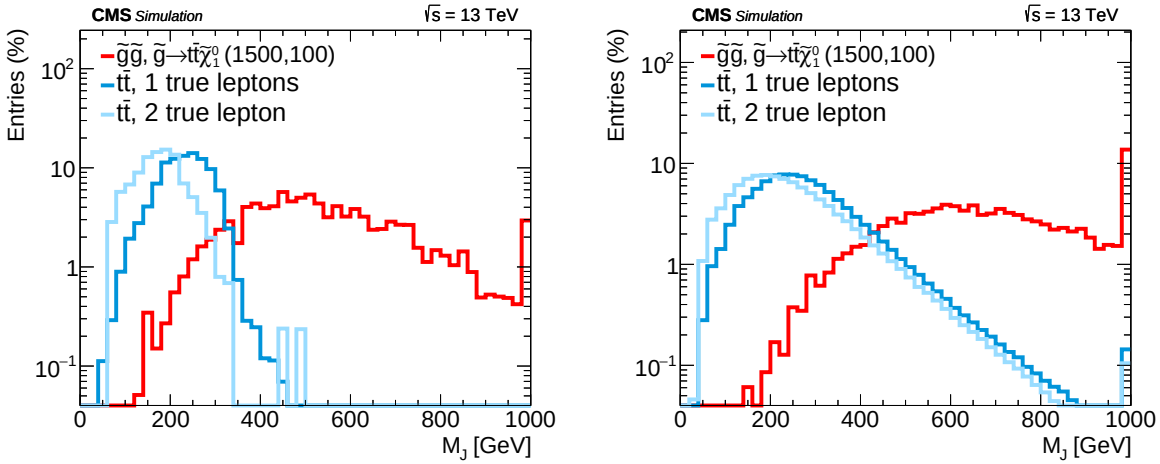

Figure 2: Distributions of M_J from simulated event samples with little ISR (left), and significant ISR (right). The amount of ISR is selected using the p_T of the $t\bar{t}$ or gluino-gluino system. The distributions are shown for $t\bar{t}$ single- and dilepton events and for a T1tttt SUSY model with a 1500 GeV gluino and a 100 GeV neutralino. When the ISR contribution is small, the M_J distribution for $t\bar{t}$ events has a cutoff around $2m_t$ (blue curves in the left-hand plot). If the ISR contribution is substantial, this tail is greatly extended (blue curves in the right-hand plot. The signal events have a large tail in the M_J distribution regardless of the amount of ISR. For each distribution, the mean value (μ) is given in the legend.

Standard R=0.4 anti-k_T jets are used to establish a correspondence between the parton shower of a single isolated quark or gluon and a jet. In events where there may be angular correlations between the quarks, e.g., in a boosted top decay, or where a large number of quarks may accidentally result in nearby showers, it has been found beneficial to cluster the event with larger radii, capturing multiple partons in the same jet. In these cases, the mass of the large-R jets retains some of the angular information, allowing one to construct variables with improved discrimination power, such as M_J. The optimal large-R jet reconstruction parameters and corresponding M_J definition for this analysis were extensively studied by comparing the background rejection vs. signal efficiency for M_J using a variety of settings. For example, the performance of large-R jets was compared for cone sizes of 0.8, 1.0, 1.2, and 1.4. For a T1tttt model with a large gluino-neutralino mass splitting, the performance is very similar, but for a compressed-spectrum T1tttt model, smaller cone sizes are preferred. However, in $t\bar{t}$ events, the mass peak from hadronic top-quark decay is best reconstructed with a cone size of 1.2, which was adopted for the analysis.

For this analysis, where the main background is $t\bar{t}$, the M_J distribution has a natural endpoint at twice the mass of the top quark for events in which no ISR jets (Fig. 2, left) are present, while the M_J distribution for signal events extends to much larger values. The $t\bar{t}$ background in the high M_J region arises from the presence of ISR, as shown in Fig. 2, right.

4 Trigger and event selection

The data sample used in this analysis was acquired using High Level Trigger (HLT) paths that require at least one lepton (an electron or a muon) satisfying $p_T > 15$ GeV, together with the requirement $H_T > 350$ GeV, where H_T is the scalar sum of the transverse momenta of the jets in the event (reconstructed online). The HLT is seeded with a Level 1 trigger that requires $H_T^{L1} > 150$ GeV.

We measured the trigger efficiency on an event sample selected with an orthogonal trigger with an online $E_{\mathrm{T}}^{\mathrm{miss}} > 170$ GeV requirement. We studied the dependence of the trigger efficiency as a function of lepton p_{T} and the analysis variables, and found efficiencies consistent with a constant value. The total trigger efficiency for events with one offline lepton, $H_{\mathrm{T}} > 500$ GeV, $N_{\mathrm{jets}} \geq 4$ and $E_{\mathrm{T}}^{\mathrm{miss}} > 200$ GeV are:

$$\epsilon_{\mu} = (95.1^{+0.5}_{-0.5} \pm 1.0)\%, \tag{6}$$

$$\epsilon_{e} = (94.1^{+0.6}_{-0.7} \pm 1.0)\%. \tag{7}$$

The second uncertainty is systematic and covers residual dependence of the trigger efficiency on lepton p_{T} and the analysis variables.

The offline event selection is described in Table 2, which lists the event yields obtained from simulation for the main SM backgounds and for the T1tttt NC (non-compressed) and T1tttt C (compressed) SUSY models, as a series of offline selection requirements is imposed. The T1tttt NC model has $m(\tilde{\mathrm{g}}) = 1500$ GeV and $m(\tilde{\chi}_1^0) = 100$ GeV, while the T1tttt C model has $m(\tilde{\mathrm{g}}) = 1200$ GeV and $m(\tilde{\chi}_1^0) = 800$ GeV. The yields in this table are normalized to an integrated luminosity of 2.1 fb^{-1}.

The first group of analysis requirements listed correspond to the baseline selection. No explicit trigger requirements are listed. However, the offline requirements are designed to be sufficiently stringent that the associated efficiency has reached its plateau value for the trigger threshold that is applied.

The requirements listed through $N_{\mathrm{b}} \geq 1$ represent the *baseline selection*, and give $S/B \approx 1\%$. Beyond the horizontal line, Table 2 lists several additional cut, together with the corresponding event yields. As discussed in the following section, the requirement $M_J > 250$ GeV is applied to ensure that the background estimation method is robust for $\mathrm{t\bar{t}}$ events. We define an analysis region in the M_J-m_{T} plane, then bin in the variables $E_{\mathrm{T}}^{\mathrm{miss}}$, N_{jets}, and N_{b}. The cuts listed below $M_J > 250$ GeV give an example of one of the analysis bins.

After the baseline selection is applied, $\mathrm{t\bar{t}}$ is the dominant background, but most of it arises from true single-lepton production. As shown in Table 2, this component is strongly suppressed by a tight m_{T} requirement, which has an efficiency $\epsilon(m_{\mathrm{T}} > 140\,\mathrm{GeV}) \approx 1\%$ for the single-lepton $\mathrm{t\bar{t}}$ contribution. The background is then dominated by dilepton $\mathrm{t\bar{t}}$. The background contributions from QCD, W + jets production, $\mathrm{t\bar{t}V}$, and "Other", are now each below the one-event level. A simple background composition dominated by a reasonably well understood source provides the basic framework for the analysis.

Figure 3 (left) shows the distributions of m_{T} after the baseline selection is applied. Dilepton $\mathrm{t\bar{t}}$ events dominate the SM background contribution for $m_{\mathrm{T}} > 140$ GeV.

Figure 3 (right) shows the corresponding distributions of M_J after the baseline selection and the $m_{\mathrm{T}} > 140$ GeV requirement are both applied. The M_J distribution shows that a broad range of signal distributions is expected, depending on how compressed the mass spectrum for the model is. Compressed-spectrum models have M_J distributions that are more similar to the $\mathrm{t\bar{t}}$ backgrounds, and we will see below that models such as T1tttt (C) can produce some signal contamination in the control regions. We have therefore used a fit of signal and control regions together to obtain the signal and background contributions.

The results from Table 2 and Fig. 3 motivate our choice of the main signal and control regions, which are the following four rectangular regions in the m_{T}-M_J plane:

- Region R1: $m_{\mathrm{T}} \leq 140$ GeV, $250 \leq M_J \leq 400$ GeV

Table 2: Event yields obtained from simulated event samples, as the event selection criteria are applied. The category *Other* includes Drell-Yan, $t\bar{t}H(\rightarrow b\bar{b})$, and WW. Hadronic $t\bar{t}$ is included in QCD. The selection requirements listed above the horizontal line in the middle of the table are defined as the baseline requirements. The equivalent luminosity of the MC samples is at least 6 times that of the data, and at least 100 times for $t\bar{t}$ and signal. Thus, rows with 0 yield have statistical uncertainties of 0.16 events at most, and below 0.05 events in most cases.

$\mathcal{L} = 2.1$ fb^{-1}	Other	QCD	$t\bar{t}V$	Single t	W+jets	$t\bar{t}$ (1ℓ)	$t\bar{t}$ (2ℓ)	SM bkg.	T1tttt NC	T1tttt C
No selection	–	–	–	–	–	–	–	–	29.1	176.0
1ℓ	–	–	–	–	–	–	–	–	11.1	63.6
$H_T > 500$ GeV	3851.8	29242.1	685.2	2694.9	29289.4	25687.5	3170.5	94621.4	11.1	41.6
MET> 200 GeV	286.6	142.4	84.7	422.2	3991.1	2054.0	565.2	7546.3	9.8	19.9
$N_{\text{jets}} \geq 6$	25.1	7.4	34.7	76.3	255.9	756.0	168.6	1323.9	8.9	18.9
$N_{\text{b}} \geq 1$	8.7	2.4	27.9	59.1	60.9	602.8	135.1	896.9	8.4	17.7
$M_J > 250$ GeV	6.2	2.4	21.3	40.5	42.3	438.0	87.5	638.2	8.4	15.3
$N_{\text{b}} \geq 2$	2.7	0.6	9.5	17.0	7.2	194.1	39.4	270.5	6.4	11.5
$m_T > 140$ GeV	0.3	0.4	1.3	1.6	0.3	2.5	14.7	21.1	5.0	6.4
$M_J > 400$ GeV	0.1	0.0	0.5	0.6	0.0	1.4	4.7	7.4	4.5	3.2
MET > 400 GeV	0.0	0.0	0.1	0.3	0.0	0.1	0.8	1.3	3.4	1.4
$N_{\text{jets}} \geq 9$	0.0	0.0	0.0	0.0	0.0	0.0	0.1	0.2	1.5	0.9
	Other	QCD	$t\bar{t}V$	Single t	W+jets	$t\bar{t}$ (1ℓ)	$t\bar{t}$ (2ℓ)	SM bkg.	T1tttt NC	T1tttt C

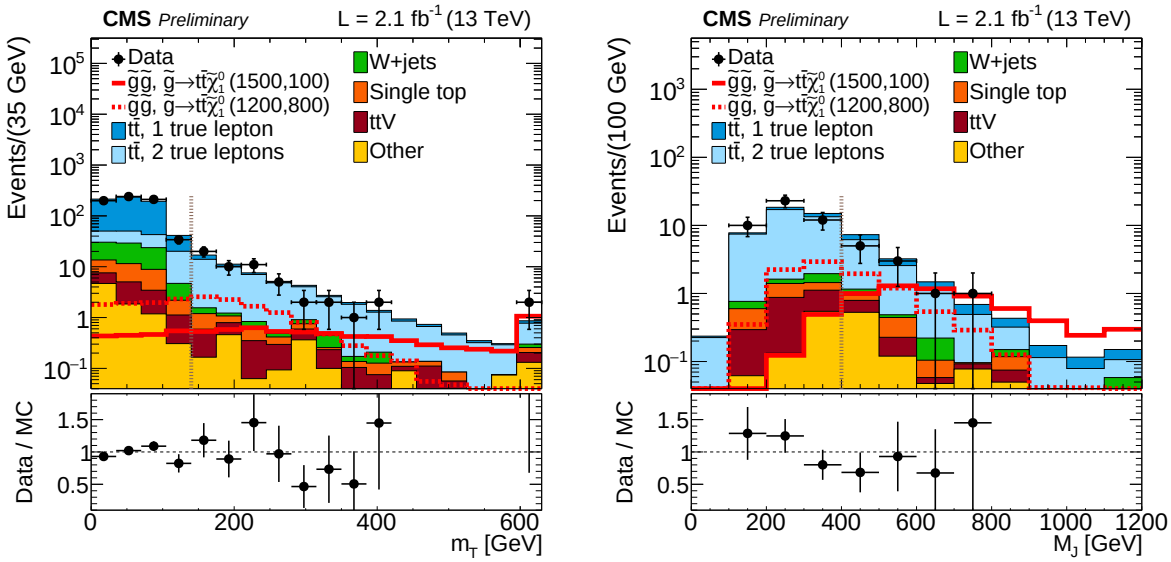

Figure 3: Distributions of m_{T} after the baseline selection is applied (left) and M_J after the baseline selection and the requirement $m_{\mathrm{T}} > 140$ GeV are applied (right).

- Region R2: $m_{\mathrm{T}} \leq 140$ GeV, $M_J > 400$ GeV
- Region R3: $m_{\mathrm{T}} > 140$ GeV, $250 \leq M_J \leq 400$ GeV
- Region R4: $m_{\mathrm{T}} > 140$ GeV, $M_J > 400$ GeV

To exploit the additional information from $E_{\mathrm{T}}^{\mathrm{miss}}$, N_{jets}, and N_{b}, each of the four regions in the m_{T}-M_J plane is itself divided into the following sub-regions:

- $E_{\mathrm{T}}^{\mathrm{miss}}$: [200, 400], [400+]
- N_{jets}: [6, 8], [9+]
- N_{b}: [1], [2], [3+]

As we explain in the following section, the binning employed in the background estimation method combines some of these sub-regions to ensure that the most sensitive bins have a few expected signal events.

5 Background estimation

5.1 Overview and kinematic properties of background events

Figure 4 shows the distribution of signal and background events in the M_J-m_{T} plane after baseline selection. In regions R1 and R2 (low m_{T}) the background is dominated by single-lepton $\mathrm{t\bar{t}}$ events, whereas in R3 and R4 (high m_{T}) the background is dominated by dilepton $\mathrm{t\bar{t}}$ events.

The prediction of the background yields in the signal region takes advantage of the fact that the kinematic variables M_J and m_{T} are largely uncorrelated. This behavior allows us to measure the m_{T} shape in data with good statistical precision in the background-dominated regions at low M_J (R1 and R3), and extrapolate into the high-M_J regions (R2 and R4). Alternatively, we can say that, with a sufficient number of jets in the events, the M_J distribution of the background in R1-R2 is nearly identical to that in R3-R4. These points are addressed in detail in this section.

As discussed in Section 4, each of the four regions is divided into bins of N_{jets}, $E_{\mathrm{T}}^{\mathrm{miss}}$, and N_{b}. The binning is shown in Fig. 5 and discussed further below.

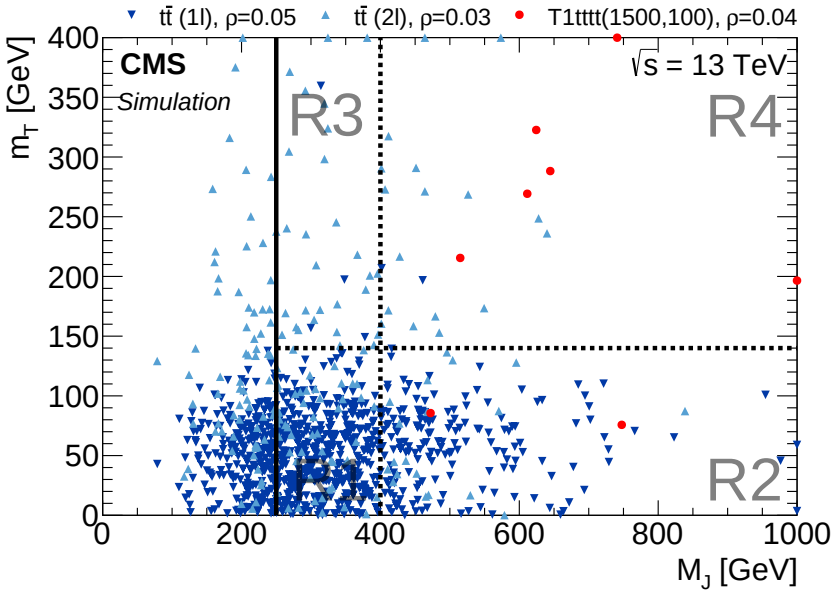

Figure 4: Distribution of single lepton $t\bar{t}$, dilepton $t\bar{t}$, and T1tttt(1500,100) events in the M_J-m_T plane after baseline selection. Each marker represents one expected event at $\mathcal{L} = 3\,\text{fb}^{-1}$. The correlation coefficients ρ are shown in the legend.

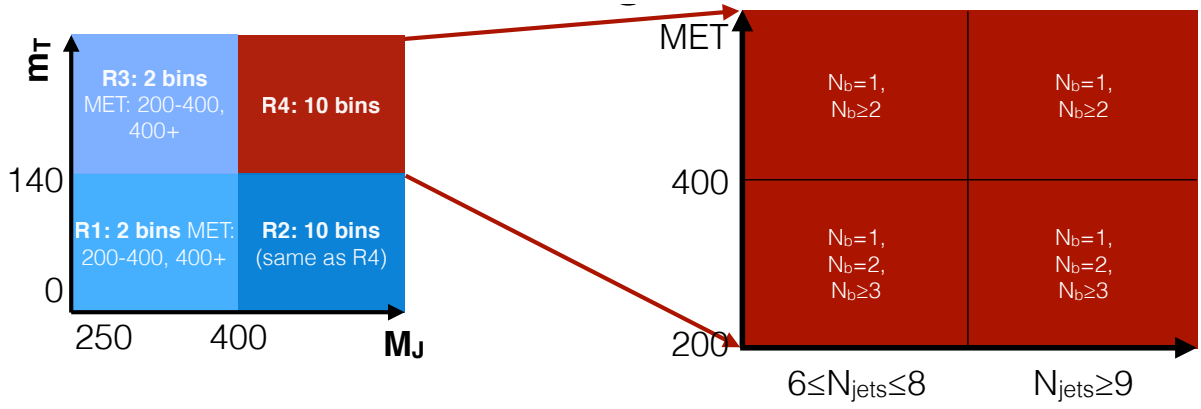

Figure 5: Binning used in the signal (R4) and control regions (R1, R2, and R3) of the analysis. The low M_J region R1 and R3 are divided only into low and high MET regions. Because of the correlation with m_T, binning in MET is necessary in the low M_J sideband to obtain the correct m_T shape. At high M_J, we partition regions R2 and R4 into 10 bins each using N_{jets}, N_b, and E_T^{miss}.

To obtain an estimate of the background rate in each of these signal bins, a modified ABCD method is used. This method makes use of the weak dependence of M_J and m_T to obtain a data-driven estimate of the background. Corrections derived from Monte Carlo are then applied in order to compensate for the small correlation between M_J and m_T. Furthermore, we estimate the background in two ways:

- a "predictive" estimate for the background in the signal region R4 in which the yield in R4 itself is not used
- a global fit to all four regions.

The two methods differ only in whether terms corresponding to R4 are included in the likelihood function.

In this section, we establish that M_J and m_T are only weakly correlated; demonstrate a simplified version of the background estimate without binning, and explain how bins are incorporated into the background estimate.

Figure 4 shows the semileptonic and dileptonic $t\bar{t}$ components (light and dark blue, respectively) each have a small correlation coefficient between M_J and m_T. This gives a preliminary hint that M_J and m_T may be generally uncorrelated in the full background. As seen in Table 2, events at high m_T are primarily from dilepton $t\bar{t}$, while those at low m_T are primarily from semileptonic $t\bar{t}$. In order for the M_J-m_T to be approximately independent, the M_J shape needs to be similar for semileptonic and dilepton $t\bar{t}$. This possibility is well-motivated in events with high ISR, where the extra neutrino in dilepton $t\bar{t}$ has a relatively smaller effect on M_J. We ensure that we operate on the high-ISR tail by requiring at least 6 jets. The comparison of the M_J distributions in the baseline selection at high and low m_T is shown in Fig. 6. The shapes agree for events with 2 true leptons and events with 1 true lepton at low m_T, but differ from the shape corresponding to events with 1 true lepton and high m_T which is distorted by the presence of jet mismeasurent and lepton mis-identification. Since the single-lepton $t\bar{t}$ contribution at high m_T is only 15%, this introduces only a small correlation between M_J and m_T which we can correct using simulation.

To test the independence of M_J and m_T with respect to each other or other kinematic variables, we define the ratios

$$R_{M_J} \equiv \frac{N(M_J > 400)}{N(M_J \leq 400)}, \qquad R_{m_T} \equiv \frac{N(m_T > 140)}{N(m_T \leq 140)}. \tag{8}$$

If M_J (m_T) is independent of a particular variable, then R_{M_J} (R_{m_T}) will be constant as a function of that variable. In Fig. 7 shows that R_{m_T} varies from about 0.06 to 0.1 across various N_{jets} and N_b bins. In order for the ABCD method to work, the R_{m_T} for a particular bin on the left-hand side of the plot at low M_J must match the R_{m_T} for the corresponding bin on the right-hand side of the plot at high M_J. For $N_{\text{jets}} \geq 6$, the two R_{m_T} values are typically within 0.01 of each other, while for $N_{\text{jets}} \leq 5$, the high-M_J value for R_{m_T} is typically higher by as much as 0.05. A similar pattern appears in Fig. 8, though the statistical uncertainties are larger. The baseline cut of $N_{\text{jets}} \geq 6$ ensures that M_J and m_T are not excessively correlated.

Finally, we can make a direct test of M_J-m_T independence using the double-ratio

$$\kappa \equiv \frac{R_{m_T}(M_J > 400)}{R_{m_T}(M_J \leq 400)}, \tag{9}$$

which should be equal to one if M_J and m_T are uncorrelated within a bin. Figure 9 shows κ for several kinematic selections. It is within approximately 10 to 20% of unity for all bins.

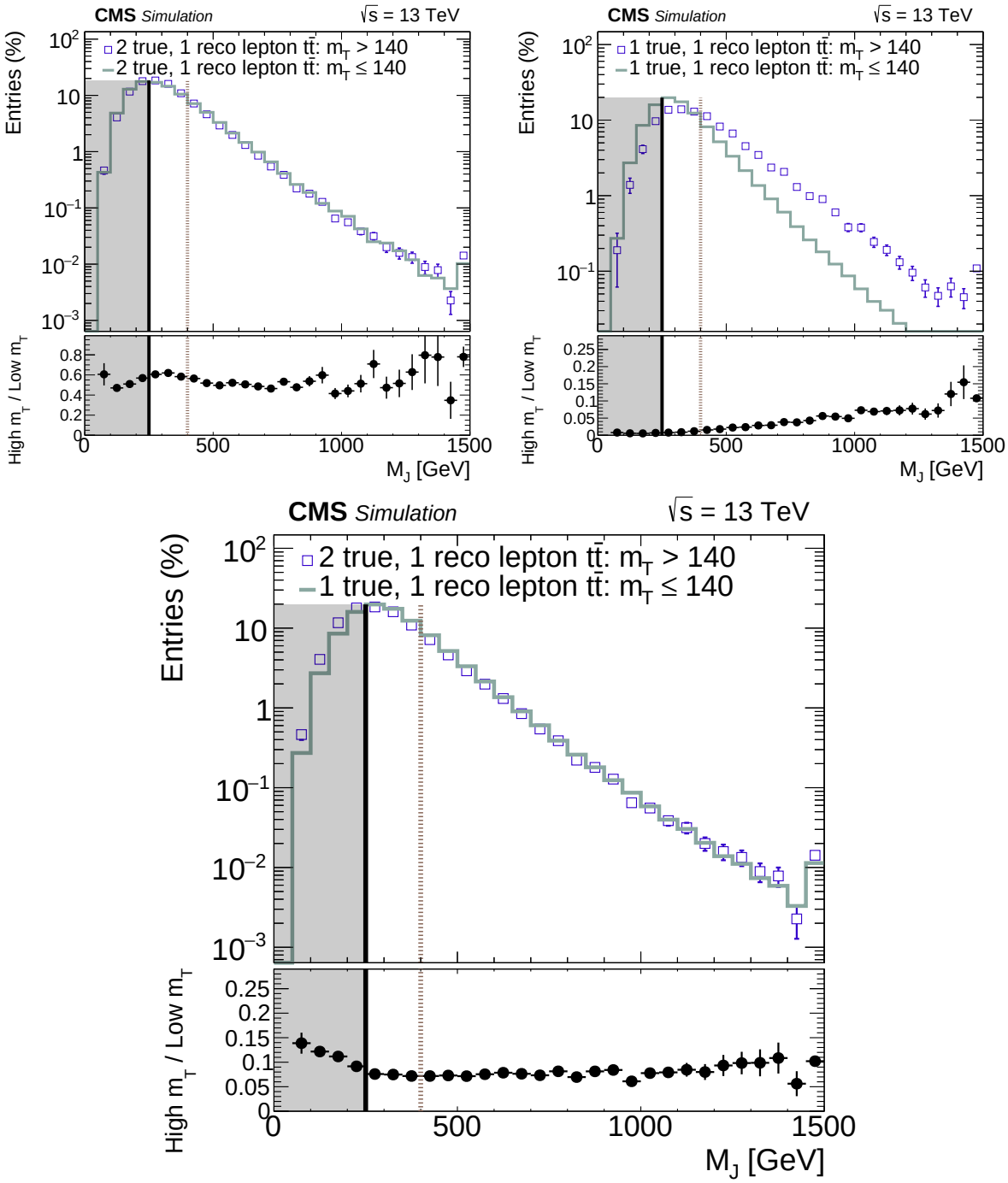

Figure 6: Top left: comparison of M_J distribution in $t\bar{t}$ events with 2 true leptons at high and low m_T. Shapes are similar. 2ℓ $t\bar{t}$ is subdominant at low m_T. Top right: comparison of M_J distribution in $t\bar{t}$ events with 1 true lepton at high and low m_T. Shapes are rather different which can introduce a correlation between M_J and m_T. However, the single lepton component of the high-m_T background is small, approximately 15% of the full sample. Bottom: comparison of M_J distribution in $t\bar{t}$ events with 2 true leptons at high m_T and 1 true lepton at low m_T. The shapes of these distributions are similar. These two are the dominant contributions to each of their respective m_T regions.

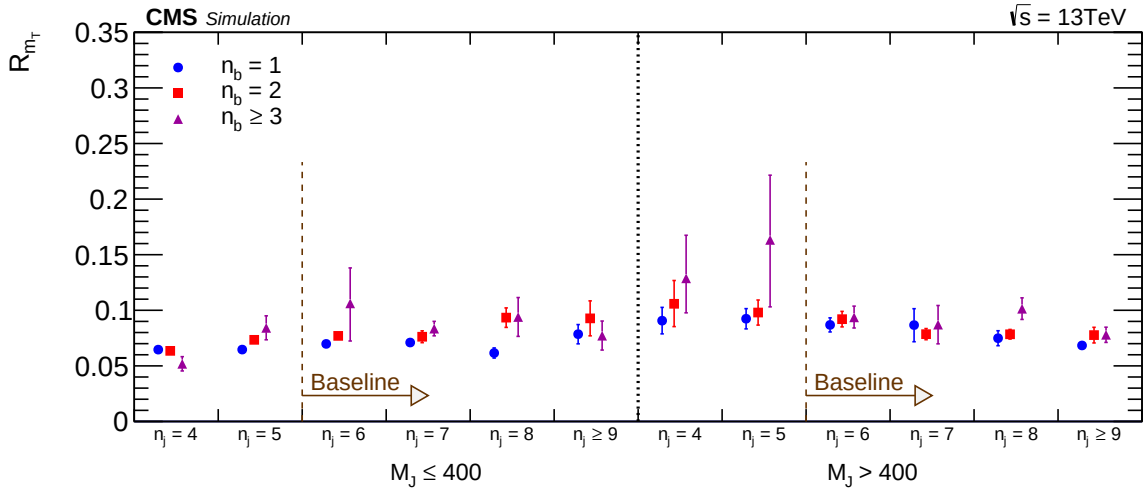

Figure 7: The high-to-low-m_T ratio R_{m_T} at low E_T^{miss} as a function of N_{jets} and N_b, showing that R_{m_T} varies slowly from approximately 0.06 to 0.1.

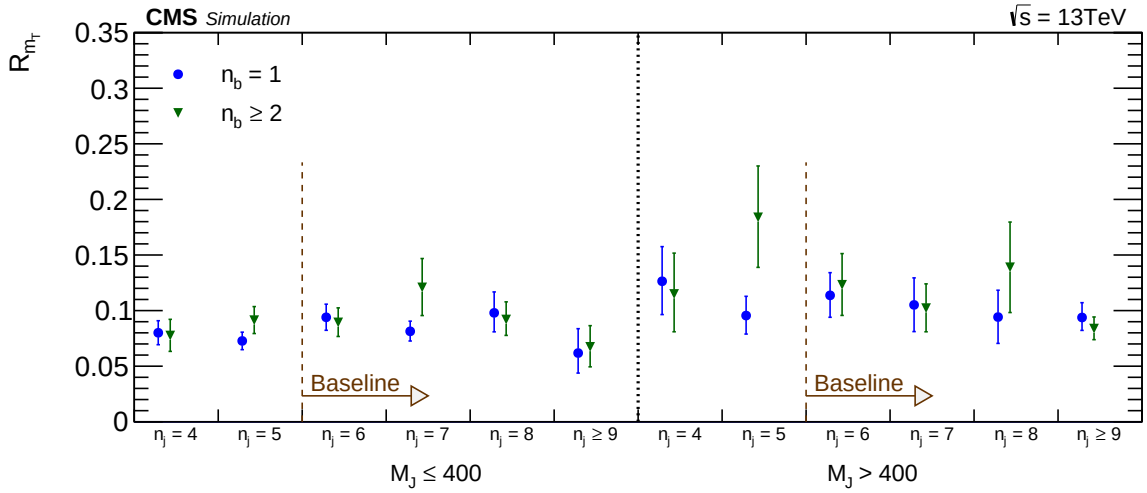

Figure 8: The high-to-low-m_T ratio R_{m_T} at high E_T^{miss} as a function of N_{jets} and N_b, showing that R_{m_T} varies slowly from approximately 0.08 to 0.12, slightly higher than the values in Figure 7. The difference between the two figures indicates a E_T^{miss} dependence in R_{m_T}.

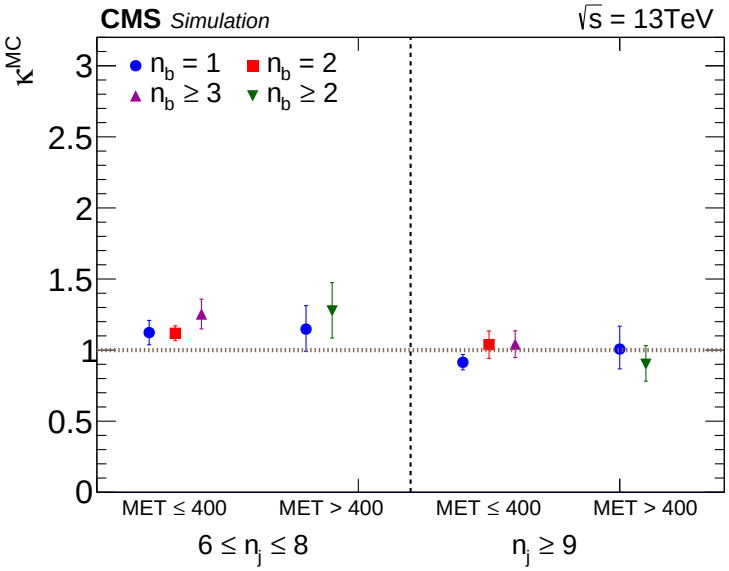

Figure 9: Double-ratio κ in various kinematic bins defined in section 4. κ is generally consistent with one, with the largest discrepancy in the bin with the tightest selection, $E_{\mathrm{T}}^{\mathrm{miss}} > 400$ and $N_{\mathrm{jets}} \geq 9$.

5.2 Background estimation procedure

5.2.1 Predicting the R4 background without the R4 yields

Before introducing binning, we have four regions in the M_J-m_{T} plane (R1, R2, R3, R4), each of which has an observed yield (N_{R1}, N_{R2}, N_{R3}, N_{R4}) and an unknown Poisson background rate ($\mu_{\mathrm{R1}}^{\mathrm{bkg}}$, $\mu_{\mathrm{R2}}^{\mathrm{bkg}}$, $\mu_{\mathrm{R3}}^{\mathrm{bkg}}$, $\mu_{\mathrm{R4}}^{\mathrm{bkg}}$). Taking M_J and m_{T} to be independent allows a data-driven estimation of the background rates. We can perform the background estimation either as a pure prediction for the background in the high-M_J, high-m_{T} region (R4), or as a global fit which incorporates the count in R4 into the likelihood function.

To obtain a pure background prediction for R4, without using the observed yield from R4, we assume that signal contamination in the sideband regions R1, R2, and R3 is negligible and that M_J and m_{T} are independent. The usual ABCD method then gives a prediction for the background rate in R4,

$$\hat{\mu}_{\mathrm{R4}}^{\mathrm{bkg}} = \frac{\hat{\mu}_{\mathrm{R2}}^{\mathrm{bkg}} \cdot \hat{\mu}_{\mathrm{R3}}^{\mathrm{bkg}}}{\hat{\mu}_{\mathrm{R1}}^{\mathrm{bkg}}}, \tag{10}$$

where $\hat{\mu}$ denotes the best estimate for the unknown true background rate μ in each bin. Ignoring potential signal contamination, the best estimate for the background in the sideband regions is the observed count, so the estimated background for signal region R4 is simply

$$\hat{\mu}_{\mathrm{R4}}^{\mathrm{bkg}} = \frac{N_{\mathrm{R2}} \cdot N_{\mathrm{R3}}}{N_{\mathrm{R1}}}. \tag{11}$$

To correct for the small correlation between M_J and m_{T}, we compute the double-ratio κ from Eq. (9) noting that κ can be expressed as

$$\kappa = \frac{\hat{\mu}_{\mathrm{R4}}^{\mathrm{MC\ bkg}}}{\frac{\hat{\mu}_{\mathrm{R2}}^{\mathrm{MC\ bkg}} \hat{\mu}_{\mathrm{R3}}^{\mathrm{MC\ bkg}}}{\hat{\mu}_{\mathrm{R1}}^{\mathrm{MC\ bkg}}}} = \frac{(\text{MC observed in R4})}{(\text{MC predicted in R4})}, \tag{12}$$

we can multiply the raw ABCD estimate in equation (11) by κ to obtain a corrected background estimate

$$\hat{\mu}_{\mathrm{R4}}^{\text{corr. bkg}} = \frac{N_{\mathrm{R2}} \cdot N_{\mathrm{R3}}}{N_{\mathrm{R1}}} \cdot \kappa. \tag{13}$$

The likelihood function in the case of a "prediction" (an estimate not using the yield in R4 itself) of the background in R4 is a product of Poisson terms,

$$\mathcal{L} = \mathcal{L}^{\text{pred}} \cdot \mathcal{L}^{\text{MC}\,\kappa}, \tag{14}$$

$$\mathcal{L}^{\text{pred}} = \prod_{i=1}^{3} \mathrm{Pois}(N_{\mathrm{R}i} | \hat{\mu}_{\mathrm{R}i}^{\text{bkg}}), \tag{15}$$

$$\mathcal{L}^{\text{MC}\,\kappa} = \prod_{i=1}^{4} \mathrm{Pois}(N_{\mathrm{R}i}^{\text{MC}} | \hat{\mu}_{\mathrm{R}i}^{\text{MC bkg}}). \tag{16}$$

The $\mathcal{L}^{\text{MC}\,\kappa}$ term accounts for the MC uncertainty on κ. In practice, this term is adjusted to account for the Monte Carlo event weights. Note that because the likelihood function already has three parameters and only three observables, the signal cannot be extracted with this approach.

5.2.2 Estimating backgrounds with a global fit

To extract the signal strength r, the observed yield N_{R4} must be used. The ABCD constraint is enforced by requiring the background shape across the four regions to have only two shape parameters $R_{m_{\mathrm{T}}}$ and R_{M_J}, and one normalization N:

$$\hat{\mu}_{\mathrm{R1}}^{\text{bkg}} = N, \qquad \hat{\mu}_{\mathrm{R2}}^{\text{bkg}} = N R_{M_J}, \tag{17}$$

$$\hat{\mu}_{\mathrm{R3}}^{\text{bkg}} = N R_{m_{\mathrm{T}}}, \qquad \hat{\mu}_{\mathrm{R4}}^{\text{bkg}} = N R_{M_J} R_{m_{\mathrm{T}}}. \tag{18}$$

We correct for M_J-m_{T} correlations by fitting to MC and finding a correction factor λ_i analagous to κ from equation (12):

$$\lambda_i \equiv \frac{(\text{MC observed in region } i)}{(\text{MC fit in region } i)}. \tag{19}$$

The corrected background estimate is just the uncorrected estimate multiplied by λ. The estimated signal rate is the Monte Carlo rate scaled by the signal strength parameter r.

The likelihood function is

$$\mathcal{L} = \mathcal{L}^{\text{fit}} \cdot \mathcal{L}^{\text{MC}\,\lambda} \cdot \mathcal{L}^{\text{MC sig}}, \tag{20}$$

$$\mathcal{L}^{\text{fit}} = \prod_{i=1}^{4} \mathrm{Pois}(N_{\mathrm{R}i} | \hat{\mu}_{\mathrm{R}i}^{\text{bkg}} + r \cdot \hat{\mu}_{\mathrm{R}i}^{\text{sig}}), \tag{21}$$

$$\mathcal{L}^{\text{MC}\,\lambda} = \prod_{i=1}^{4} \mathrm{Pois}(N_{\mathrm{R}i}^{\text{MC}} | \hat{\mu}_{\mathrm{R}i}^{\text{MC bkg}}), \tag{22}$$

$$\mathcal{L}^{\text{MC sig}} = \prod_{i=1}^{4} \mathrm{Pois}(N_{\mathrm{R}i}^{\text{MC}} | \hat{\mu}_{\mathrm{R}i}^{\text{MC sig}}), \tag{23}$$

where $\mathcal{L}^{\text{fit}}$ accounts for the statistical uncertainty from the fit to data, $\mathcal{L}^{\text{MC}\,\lambda}$ accounts for uncertainty in the computation of the λ correction factors, and $\mathcal{L}^{\text{MC sig}}$ accounts for uncertainty in the signal shape due to the finite size of the Monte Carlo sample.

5.3 Binning in N_{jets}, $E_{\text{T}}^{\text{miss}}$, and N_{b}

As discussed in Section 4, we bin the M_J-m_{T} regions in N_{jets}, $E_{\text{T}}^{\text{miss}}$, and N_{b} in order to improve the expected sensitivity. In principle, one could use the same bins in all four regions R1, R2, R3, and R4 and conduct a separate ABCD background estimate in each of the bins. However, this provides limited yields in the sideband regions R1 and R3 and results in large statistical uncertainties.

To improve statistical precision, we integrate R1 and R3 over N_{jets} and N_{b} and assume that the bins all share a common $R_{m_{\text{T}}}$. As long as $R_{m_{\text{T}}}$ is the same at low and high M_J, the fit shape will correctly model the background. We note that the low M_J bins in the left halves of Figures 7 and 8 and the high M_J bins in the right halves have similar shapes, indicating that this condition is met. Figures 7 and 8 show that $R_{m_{\text{T}}}$ is nearly constant as a function of N_{jets} and N_{b}, varying between about 0.07 and 0.1 for most bins, indicating that the systematic error introduced by assuming they share a common $R_{m_{\text{T}}}$ is small. Finally, because the variation in $R_{m_{\text{T}}}$ is both small and gradual, we rely on the Monte Carlo to correct for this variation.

The background estimation procedure has a separate ABCD fit for the low and high $E_{\text{T}}^{\text{miss}}$ sets of bins sharing only the signal strength parameter r. Both fits have their own $R_{m_{\text{T}}}$ and background normalization N, and a separate R_{M_J} for each bin in region R2 and R4.

6 Systematic uncertainties

6.1 Background uncertainties

The uncertainty on the background prediction can be separated into two components: the statistical uncertainty on the event yields in each of the ABCD regions, which is incorporated into the background fit, and the systematic uncertainties on the MC-derived corrections for bias of the method.

The correction to a simple ABCD background prediction are quantified in terms of the quantitiy κ, the correction factor used when a background prediction is obtained without using the R4 yields. The uncertainties on κ arise from various effects, such as modeling of initial-state radiation. We study the uncertainty that results from specific sources of mis-modeling by introducing variations into the MC and determining the resulting change in κ. When the background is instead estimated via a global fit, the uncertainties are supplied to the fit as additional uncertainties on the yield in Region 4.

In addition to the specifically motivated uncertainties, we determine a systematic uncertainty from potential bias of the method in a data validation sample. An analogous ABCD method is used to predict the yield in signal-free regions of a dilepton validation sample. This test provides a quantitative test of the method in data using essentially the same type of events that feed down to the single-lepton sample and generate the dominant background in the analysis.

The uncertainties are summarized in Table 3. We discuss the methods used to determine these uncertainties below.

As noted in section 2, in 8 TeV data, the top p_{T} distribution [43] was observed to be softer than predicted by MC. This observation is compatible with early 13 TeV studies. This motivates using the 8 TeV measurement to reweight the $\text{t}\bar{\text{t}}$ sample to achieve better agreement with data. Since top p_{T} modeling is a factor in determining M_J in $\text{t}\bar{\text{t}}$ events, we take the full shift in κ when comparing the $\text{t}\bar{\text{t}}$ sample before and after this reweigting as a systematic uncertainty. We find that the effect on κ is limited to 1–4% across all analysis bins.

Table 3: Summary of fractional uncertainties on κ. The systematic uncertainties are symmetrized. Statistical uncertainties are estimated from the predictive fit to 2.1 fb^{-1} of data.

Uncertainty [%]	$6 \leq N_{jets} \leq 8$					$N_{jets} \geq 9$				
	$200 \leq MET \leq 400$			$MET > 400$		$200 \leq MET \leq 400$			$MET > 400$	
	$N_b = 1$	$N_b = 2$	$N_b \geq 3$	$N_b = 1$	$N_b \geq 2$	$N_b = 1$	$N_b = 2$	$N_b \geq 3$	$N_b = 1$	$N_b \geq 2$
Data stat. ($\mathcal{L} = 2.1\,fb^{-1}$)	28	28	37	68	81	46	45	117	115	114
	Systematic uncertainties associated with MC mis-modeling									
ISR p_T	4	4	4	5	4	3	4	4	7	5
top p_T	< 1	< 1	< 1	< 1	3	< 1	< 1	< 1	4	< 1
jet resolution	4	4	13	4	4	3	3	17	2	2
JEC	1	2	1	4	2	4	2	5	3	4
non-$t\bar{t}$	2	3	4	6	11	8	2	4	11	2
κ stat.	7	4	8	10	12	5	9	9	10	8
2ℓ test ($\mathcal{L} = 2.1\,fb^{-1}$)	37					90				

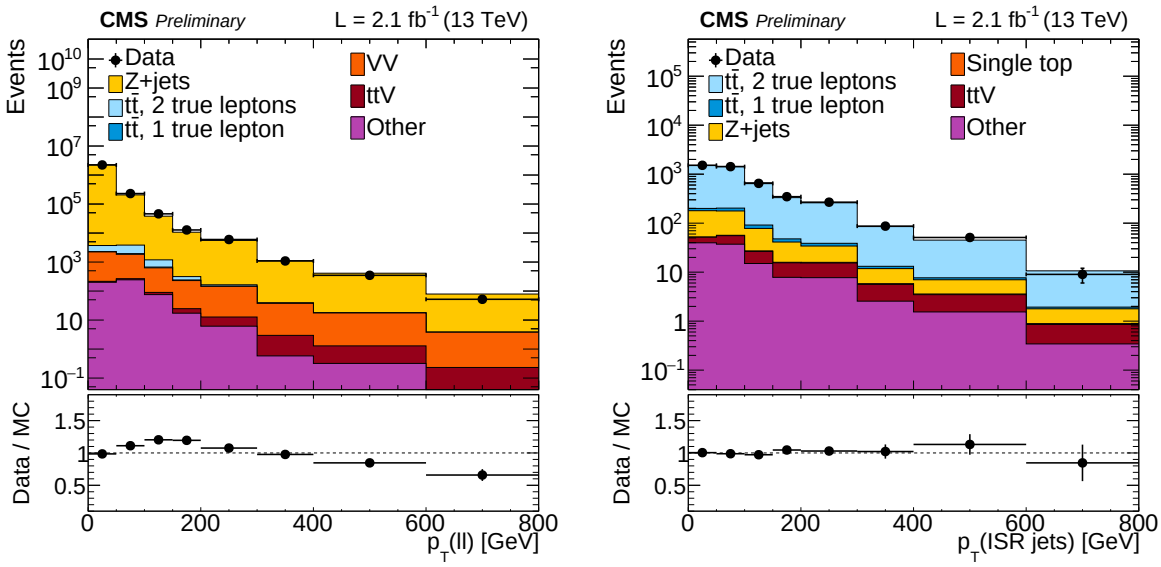

Figure 10: The ISR p_T in Z + jets sample (left) and a dilepton $t\bar{t}$ sample(right).

Similarly to the top p_T, the ISR p_T [44] distribution has been shown to be softer than predicted by MC at 8 TeV. The modeling of the ISR p_T at 13 TeV is studied in two samples Z + jets and dilepton $t\bar{t}$. In the Z + jets sample, events are selected by requiring two opposite-sign same-flavor leptons with invariant mass between 80 and 100 GeV. The p_T of the dilepton system, in this case the Z p_T, is then equal to the ISR p_T. In the $t\bar{t}$ sample, events are selected by requiring exactly two leptons and exactly 2 b-tagged jets. This selection makes it possible to single out the system of jets, excluding the 2 b-jets coming from the top decays, which can then be identified with the ISR p_T in the event. The data to MC comparison for both samples is shown in Fig. 10. In Z + jets events, the MC underestimates the fraction of events with 100-200 GeV ISR p_T, and overestimates the fraction with more than 400 GeV ISR p_T. In $t\bar{t}$ events, the ISR p_T in data and MC agree within the statistical uncertainty. While the $t\bar{t}$ sample directly represents the physical process dominating our analysis selection, the ISR p_T measurement at high ISR p_T is more precise in the Z + jets sample. Therefore, to assign a conservative estimate on the impact of a potential ISR p_T mismodeling at high ISR p_T on our background prediction we scale down the $t\bar{t}$ sample by 15% for events with $t\bar{t}$-system p_T between 400 and 600 GeV, and 30% for $t\bar{t}$-system p_T 600 GeV and above. Using this reweighted sample, we measure the shift in κ with respect to its nominal value. The resulting uncertainty ranges between 3 and 7%.

A source of bias of the ABCD in the M_J-m_T plane is the difference between the shape in the M_J distribution for single lepton $t\bar{t}$ events in the low- and high-m_T regions. To understand the systematic effects on how well the MC models this difference requires an understanding of how these events can populate the $m_T > 140$ region. In semileptonic $t\bar{t}$, this can only occur due to reconstruction effects or extra E_T^{miss} from non-prompt neutrinos. These high-m_T events can be grouped into three categories.

Lost-Fake Lepton events: In simulation, a truth-matched, W-associated lepton is not selected (or is a hadronic tau), and instead a fake lepton is reconstructed as the signal lepton. There is then no correlation between the E_T^{miss} and lepton, and an event can be reconstructed with high m_T. These events, however, do have a similar M_J shape as that in low-m_T semi-leptonic $t\bar{t}$ and therefore do not introduce any ABCD non-closure. This is because the lost lepton (especially in the case of hadronic taus) can still be clustered in the fatjets.

Jet Mismeasurement is the dominant contribution to the high-m_T, semileptonic $t\bar{t}$ events. When a

jet is mismeasured, it introduces fake $E_{\mathrm{T}}^{\mathrm{miss}}$ and thereby moves low-m_{T} events to high-m_{T}. These cases are identified by selecting events with $m_{\mathrm{T}} \leq 140$ when calculated with generator-level quantities, but $m_{\mathrm{T}} > 140$ with reconstruction-level quantities. Since the p_{T} mismeasurement propagates into M_J such events do result in different M_J shape at low and high m_{T}.

Non-Prompt Neutrinos add additional real $E_{\mathrm{T}}^{\mathrm{miss}}$, which can lead to high-m_{T}. These events have $m_{\mathrm{T}} > 140$ for both reconstruction- and generator-level quantities. Even though these can affect the M_J shape their contribution is small and should be well modeled by MC.

Given this categorization, any systematic mismodeling should be largely due to the *Jet mismeasurement* category. We quantify the potential effects by smearing jets by an amount that is 150% of the jet energy resolution correction factors measured in 8 TeV. Additionally, if any jet's reconstructed energy is on the tail of the resolution function, the event is weighted up by a factor of 1.5. This resolution smearing increases the fraction of high m_{T} events from semileptonic $\mathrm{t\bar{t}}$ by 33%. If there were no difference in the M_J shape, this change of m_{T} would have no effect on κ. However, as seen in Fig. 6, mismeasured single lepton events do have a different M_J shape, and the resulting change in κ reaches up to 17% as shown in Table 3.

We also propagated the uncertainties on the jet energy corrections (JEC) onto all the analysis variables, like $E_{\mathrm{T}}^{\mathrm{miss}}$, m_{T}, or M_J. We then assessed their impact on the κ factors to be less than 5%.

Finally, the modeling of non-$\mathrm{t\bar{t}}$ background was assessed in control samples rich in these processes, such as $N_{\mathrm{b}} = 0$ for W+jets or dilepton at low $E_{\mathrm{T}}^{\mathrm{miss}}$ and N_{b} for Drell-Yan. We studied the agreement between MC and data for m_{T}, M_J, and the variables in which the analysis is binned, and observed agreement always within 100%. Since the non-$\mathrm{t\bar{t}}$ component is fairly small, we assign a this 100% as its systematic uncertainty.

6.1.1 Test in data with the dilepton validation region

In addition to these specific, identifiable sources of uncertainty on κ, we obtain an uncertainty using the dilepton sample in data. This is a powerful test, but because of the limited size of the dilepton sample, it generates the largest of all the systematic uncertainties listed in Table 3.

To measure the uncertainty, the background fit is carried out in the validation ABCD plane. The low-m_{T} half remains the same as in the prediction for the 1ℓ signal region. The high-m_{T} half is replaced by 2ℓ events without an m_{T} requirement. We choose this combination of regions because it closely resembles the actual background estimate, for which the low-m_{T} region is dominated by single lepton events, while the high-m_{T} events are dominated by dilepton events with a lost lepton.

To ensure closer correspondence between the validation and search regions, the large radius jets in both samples should be clustered from the same number of constituent objects, since this number affects the M_J distribution. Since we include leptons in the clustering, the dilepton N_{jets} requirement must be reduced by 1 in all bins to compensate for the additional lepton. To improve the statistical precision of the test, we include dilepton events with N_{b} = 0, 1 or 2, but we exclude $N_{\mathrm{b}} \geq 3$ to avoid signal contamination. The uncertainty for $N_{\mathrm{b}} \geq 3$ is taken to be equal to the one found in $N_{\mathrm{b}} = 2$.

Figure 11 compares the shape of the distribution of M_J for single-lepton events with $m_{\mathrm{T}} < 140\,\mathrm{GeV}$ events (regions R1 and R2) with that for di-lepton events (regions D3 and D4). Although statistics in the di-lepton sample are limited, the shapes are in agreement.

The uncertainty is assessed in the two N_{jets} bins in D4 by comparing the dilepton background

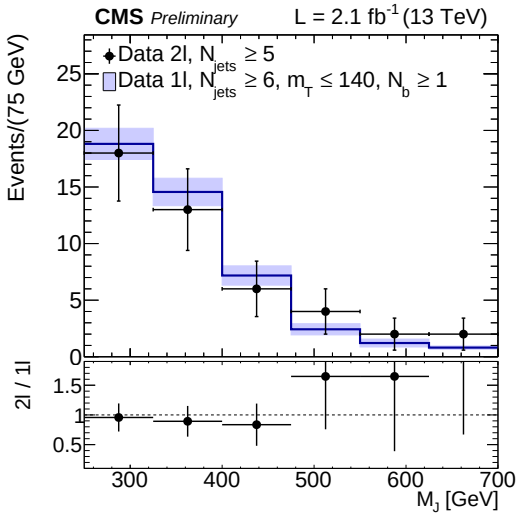

Figure 11: Uncertainty measurement using the dilepton sample in data (2.1 fb^{-1}). Distribution of M_J for single-lepton $m_{\mathrm{T}} < 140\,\mathrm{GeV}$ (blue histogram) and di-lepton events (black points with error bars). The overall yield from the singe-lepton events is normalized to that for the di-lepton sample to compare shapes.

prediction with the yield in data, Table 4. For $5 \leq N_{\mathrm{jets}} \leq 7$, this method predicts 11.1 ± 2.4 events and we observe 12. For $N_{\mathrm{jets}} \geq 8$, the prediction is 1.4 ± 0.5 and we observe 2. The good agreement between predictions and observations validates the method. The statistical precision of this test, evaluated as the sum in quadrature of the uncertainty on the prediction and the square root of the prediction, is taken as a systematic uncertainty. This results in 37% a low N_{jets} and 90% at high N_{jets}.

6.2 Uncertainties on the signal yield

The systematic uncertainties in the signal yield arise from both experimental and theoretical effects. Each systematic uncertainty is evaluated in the 24 bins separately, and they are treated as symmetric log-normal. In case that the sizes of up and down variations are not the same, the variation having larger absolute value is taken. If the sign of variations changes bin-by-bin, the correlation between bins are preserved, while the value which has the larger absolute variation is taken. A summary of the magnitude of the uncertainty due to each systematic source for the two signal model points is shown in Table 5. The uncertainties on lepton reconstruction and

Table 4: The result of the background prediction from the predictive fit to 2.1 fb^{-1} of data. Data yields in R1 and R2 (single-lepton events) and D3 and D4 (di-lepton events), and the predicted background in each region are shown. The R2 and D4 regions are divided into two bins in N_{jets}, $6 \leq N_{\mathrm{jets}} \leq 8$ and $N_{\mathrm{jets}} \geq 9$ for R2, and $5 \leq N_{\mathrm{jets}} \leq 7$ and $N_{\mathrm{jets}} \geq 8$ for D4. The uncertainty on the κ factors only include MC statistics.

	κ	Bkg. Pred.	Observed
R1: $m_T \leq 140, M_J \leq 400$	–	330.1 ± 18.2	330
R2: $6 \leq N_{\mathrm{jets}} \leq 8, m_T \leq 140, M_J > 400$	–	100.9 ± 10.0	101
R2: $N_{\mathrm{jets}} \geq 9, m_T \leq 140, M_J > 400$	–	14.0 ± 3.7	14
D3: $M_J \leq 400$	–	31.0 ± 5.6	31
D4: $5 \leq N_{\mathrm{jets}} \leq 7, M_J > 400$	1.17 ± 0.03	11.1 ± 2.4	12
D4: $N_{\mathrm{jets}} \geq 8, M_J > 400$	1.08 ± 0.04	1.4 ± 0.5	2

b-jet identification efficiencies are split into two components, one coming from the uncertainty on the efficiency when using standard detector simulation and a second factor indicating the larger unceratainty associated with the use of Fast Simulation employed in the signal sample production.

The luminosity, PU-reweighting, lepton selection scale-factor, trigger efficiency, JEC and b-tagging scale-factors contribute to the experimental effects. The uncertainties on the luminosity and PU-reweighting are 5% and 5%. The contribution from the trigger efficiency is 1%. The JEC uncertainty ranges up to 14% in R4 in the $E_{\mathrm{T}}^{\mathrm{miss}} > 400\,\mathrm{GeV}$ bins. The uncertainty on b-tagging scale-factor is estimated for the heavy quarks (b and c), and light quarks (u, d, and s) and gluons separately. The combined uncertainty is dominated by the scale-factor for heavy quarks which ranges up to 15% in R4 in the $E_{\mathrm{T}}^{\mathrm{miss}} > 400\,\mathrm{GeV}$ bins.

The renormalization and factorization scales, PDFs and ISR modeling contribute to the theoretical effects. The scales are varied up and down by a factor of 2, but in all cases constrained to be no more than a factor of 2 from each other. For these uncertainties, the up and down variations are rescaled to keep cross-section constant, *i.e.*, they are applied as shape systematic uncertainties. The uncertainty on the acceptance due to the imperfect knowledge of the parton distribution functions (PDFs) is assessed with 100 variations of the PDFs provided by NNPDF, with each variation normalized to the NNLO+NNLL cross-section. The RMS of the resulting yields in the various analysis bins is of the order of 10%, which we assign as an uncorrelated systematic uncertainty. Based on the ISR p_{T} measurement in Fig. 10, the uncertainties of 0, 15, and 30% are applied to the following ranges of p_{T} of the gluino-gluino system ($p_{\mathrm{T}}(\widetilde{\mathrm{g}}\widetilde{\mathrm{g}})$), $0 < p_{\mathrm{T}}(\widetilde{\mathrm{g}}\widetilde{\mathrm{g}}) < 400\,\mathrm{GeV}$, $400 < p_{\mathrm{T}}(\widetilde{\mathrm{g}}\widetilde{\mathrm{g}}) < 600\,\mathrm{GeV}$ and $p_{\mathrm{T}}(\widetilde{\mathrm{g}}\widetilde{\mathrm{g}}) > 600\,\mathrm{GeV}$. This has a small effect for the non-compressed mass points, but has a large effect for the compressed mass points, particularly at the high $E_{\mathrm{T}}^{\mathrm{miss}}$ region where large ISR is present.

7 Results and interpretation

Table 6 summarizes the event yields across all of the analysis bins. The rows labeled R4 contain the predicted and observed yields in each of the 10 signal regions. The background predictions from the predictive fit (PF) are obtained by fitting the three control regions, R1, R2, and R3, as described in Sec. 5. The global fit (GF) incorporates region R4 and, thus, can account for signal contamination in all regions. The κ correction factors and the yields from simulated signal event samples for the two T1tttt benchmark scenarios are also included in Table 6 for reference.

The systematic uncertainties discussed in Sec. 6 are included in the uncertainties on the prediction, including the results of the test performed using the dilepton control sample.

For the $N_{\mathrm{b}} = 1$ bins, we predict 3.4 ± 1.0 events at low $E_{\mathrm{T}}^{\mathrm{miss}}$ and low N_{jets} and observe 6. At low $E_{\mathrm{T}}^{\mathrm{miss}}$ and high N_{jets} the prediction is 0.3 ± 0.3 with 1 event observed. The high $E_{\mathrm{T}}^{\mathrm{miss}}$, $N_{\mathrm{b}} = 1$ results are predictions of 2.4 ± 1.9 and 0.3 ± 0.3 for low and high N_{jets}, respectively, with observations of 0 and 1 event. The large fractional uncertainties are driven by the number of events in the control regions, notably the R3 region.

For the more sensitive bins with $N_{\mathrm{b}} \geq 2$, we predict a combined 4.6 ± 1.3 at low $E_{\mathrm{T}}^{\mathrm{miss}}$ and 1.2 ± 0.9 at high $E_{\mathrm{T}}^{\mathrm{miss}}$ and observed 2 and 0 events, respectively. In the most sensitive bin with high $N_{\mathrm{jets}} >= 9$ and $E_{\mathrm{T}}^{\mathrm{miss}} > 400$, we predict 0.2 ± 0.3 and observe zero events. No evidence for any significant excess event yield is observed.

The results are presented graphically in several ways. Figure 12 shows the 2-dimensional distributions of m_{T} versus M_J for the $N_{\mathrm{b}} = 1$ and $N_{\mathrm{b}} \geq 2$ regions and compares them to the

Table 5: Summary of the signal systematic uncertainties. The sign of each uncertainty correponds to the impact on the yields of the upward variation of the uncertainty source. A negative sign indicates an anti-correlation with respect to bins with a positive sign. Uncertainties due to a particular source are considered fully correlated between bins, while unceratinties due to different sources are considered uncorrelated.

Uncertainty [%]	$7 \leq N_{\text{jets}} \leq 8$					$N_{\text{jets}} \geq 9$				
	$200 \leq \text{MET} \leq 400$			$\text{MET} > 400$		$200 \leq \text{MET} \leq 400$			$\text{MET} > 400$	
	$N_{\text{b}} = 1$	$N_{\text{b}} = 2$	$N_{\text{b}} \geq 3$	$N_{\text{b}} = 1$	$N_{\text{b}} \geq 2$	$N_{\text{b}} = 1$	$N_{\text{b}} = 2$	$N_{\text{b}} \geq 3$	$N_{\text{b}} = 1$	$N_{\text{b}} \geq 2$
	Signal model: T1tttt(1500,100)									
Lepton efficiency	1	1	1	1	1	1	1	1	1	1
FastSim lepton efficiency	6	6	6	6	6	6	6	6	5	6
Trigger efficiency	1	1	1	1	1	1	1	1	1	1
B-tag efficiency	-11	-1	12	-11	5	-13	-4	10	-14	3
FastSim b-tag efficiency	-4	-1	3	-4	1	-4	-1	2	-4	-1
Mistag efficiency	< 1	< 1	< 1	< 1	< 1	-1	< 1	< 1	-1	< 1
FastSim mistag efficiency	<1	<1	2	<1	1	< 1	< 1	2	-1	1
Jet energy corrections	-5	-2	-2	< 1	-2	2	2	1	6	5
PDFs	10	10	10	10	10	10	10	10	10	10
QCD scales	< 1	< 1	< 1	< 1	< 1	-1	-1	< 1	-1	-1
ISR	< 1	< 1	< 1	< 1	< 1	2	1	1	3	2
Pile up	5	5	5	5	5	5	5	5	5	5
Luminosity	5	5	5	5	5	5	5	5	5	5
	Signal model: T1tttt(1200,800)									
Lepton efficiency	1	1	1	1	1	1	1	1	1	1
FastSim lepton efficiency	6	6	6	5	5	6	6	6	5	6
Trigger efficiency	1	1	1	1	1	1	1	1	1	1
B-tag efficiency	-8	-1	8	-8	4	-9	-3	8	-11	2
FastSim b-tag efficiency	-2	< 1	1	-2	1	-2	-1	1	-3	< 1
Mistag efficiency	< 1	< 1	1	< 1	1	< 1	< 1	< 1	< 1	< 1
FastSim mistag efficiency	< 1	< 1	2	-1	1	-1	1	2	< 1	< 1
Jet energy corrections	12	-7	-10	-9	< 1	5	10	14	6	9
PDFs	10	10	10	10	10	10	10	10	10	10
QCD scales	< 1	< 1	-1	-3	-3	-2	-2	-2	-3	-3
ISR	1	1	2	23	25	2	4	2	27	25
Pile up	5	5	5	5	5	5	5	5	5	5
Luminosity	5	5	5	5	5	5	5	5	5	5

Table 6: Results of the predictive fit (PF) and global fit (GF) to 2.1 fb^{-1} of data. Sig. NC refers to the bechmark point T1tttt(1500,100), and Sig. C to T1tttt(1200,800). The first uncertainty on κ corresponds to MC statistics, and the second corresponds to the total systematic uncertainty.

Bin	κ	Sig. NC	Sig. C	Bkg. Pred. (PF)	Bkg. Pred. (GF)	Obs.
$200 < \text{MET} \leq 400$ GeV						
R1: all n_j, n_b	–	0.1	2.9	330.1 ± 18.2	329.4 ± 18.0	330
R2: $6 \leq n_j \leq 8, n_b = 1$	–	0.1	0.2	47.1 ± 6.9	49.4 ± 6.8	47
R2: $n_j \geq 9, n_b = 1$	–	0.1	0.3	6.0 ± 2.4	6.6 ± 2.5	6
R2: $6 \leq n_j \leq 8, n_b = 2$	–	0.1	0.3	42.0 ± 6.5	41.0 ± 6.2	42
R2: $n_j \geq 9, n_b = 2$	–	0.1	0.5	7.0 ± 2.6	6.5 ± 2.5	7
R2: $6 \leq n_j \leq 8, n_b \geq 3$	–	0.1	0.2	12.0 ± 3.5	11.1 ± 3.2	12
R2: $n_j \geq 9, n_b \geq 3$	–	0.1	0.6	1.0 ± 1.0	0.9 ± 0.9	1
R3: all n_j, n_b	–	0.2	3.5	21.0 ± 4.6	21.6 ± 4.2	21
R4: $6 \leq n_j \leq 8, n_b = 1$	$1.12 \pm 0.09 \pm 0.42$	0.2	0.2	3.4 ± 1.4	3.6 ± 1.0	6
R4: $n_j \geq 9, n_b = 1$	$0.91 \pm 0.05 \pm 0.82$	0.1	0.3	0.3 ± 0.3	0.4 ± 0.2	1
R4: $6 \leq n_j \leq 8, n_b = 2$	$1.12 \pm 0.05 \pm 0.42$	0.3	0.3	3.0 ± 1.2	3.0 ± 0.8	2
R4: $n_j \geq 9, n_b = 2$	$1.04 \pm 0.10 \pm 0.94$	0.3	0.6	0.5 ± 0.3	0.4 ± 0.2	0
R4: $6 \leq n_j \leq 8, n_b \geq 3$	$1.25 \pm 0.11 \pm 0.75$	0.3	0.3	1.0 ± 0.5	0.9 ± 0.3	0
R4: $n_j \geq 9, n_b \geq 3$	$1.04 \pm 0.09 \pm 0.96$	0.3	0.7	0.1 ± 0.1	0.1 ± 0.1	0
$\text{MET} > 400$ GeV						
R1: all n_j, n_b	–	0.1	0.4	15.0 ± 3.9	16.2 ± 3.9	15
R2: $6 \leq n_j \leq 8, n_b = 1$	–	0.1	0.1	8.0 ± 2.8	6.7 ± 2.5	8
R2: $n_j \geq 9, n_b = 1$	–	0.1	0.2	1.0 ± 1.0	1.7 ± 1.2	1
R2: $6 \leq n_j \leq 8, n_b \geq 2$	–	0.4	0.2	3.0 ± 1.7	2.5 ± 1.4	3
R2: $n_j \geq 9, n_b \geq 2$	–	0.4	0.5	1.0 ± 1.0	0.9 ± 0.9	1
R3: all n_j, n_b	–	0.4	0.8	4.0 ± 2.0	2.8 ± 1.4	4
R4: $6 \leq n_j \leq 8, n_b = 1$	$1.15 \pm 0.17 \pm 0.44$	0.6	0.2	2.4 ± 1.9	1.2 ± 0.7	0
R4: $n_j \geq 9, n_b = 1$	$1.01 \pm 0.15 \pm 0.92$	0.4	0.3	0.3 ± 0.3	0.3 ± 0.3	1
R4: $6 \leq n_j \leq 8, n_b \geq 2$	$1.28 \pm 0.19 \pm 0.50$	1.8	0.4	1.0 ± 0.9	0.5 ± 0.4	0
R4: $n_j \geq 9, n_b \geq 2$	$0.90 \pm 0.13 \pm 0.81$	1.5	0.9	0.2 ± 0.3	0.1 ± 0.1	0

expected signal yields for T1tttt(1500,100).

Figures 13 and 14 show the m_T and M_J distributions for $N_b = 1$. MC/data comparisons are shown as well as data/data comparisons across the ABCD plane. In the $m_T \sim 100 - 200$ GeV region of Fig. 13, 3 data bins of the m_T distribution for high M_J exceed the expectations from low M_J data and the χ^2 for this plot[1] has a p-value of only 0.2%. The p-values for χ^2 calculated with bins twice and half as wide are significantly larger, 1.5% and 13.1% respectively. The distribution with narrower bins and the comparison with MC suggests that the high M_J data might have fluctuated low for $m_T < 100$ GeV, thus pushing up the tail in the area-normalized comparisons.

Similarly, Figs. 15 and 16 show the m_T and M_J distributions for $N_b \geq 2$ and good agreement in the data/data comparisons is observed, including in the $m_T \sim 100 - 200$ GeV region. Fig. 17 shows the distributions of E_T^{miss} and N_{jets} for high and low m_T.

Figure 18 shows scans of the signal efficiency and yields in R4 in the $m(\tilde{g}) - m(\tilde{\chi}_1^0)$ plane. Finally, Fig. 19 presents the region of the $m(\tilde{g}) - m(\tilde{\chi}_1^0)$ plane that is excluded at the 95% confidence level. For low $\tilde{\chi}_1^0$ mass we exclude $\tilde{g}$ with masses of up to 1575 GeV. The highest limit on the $\tilde{\chi}_1^0$ mass is 775 GeV, reached for$m(\tilde{g})$ of approximately 1300 GeV. The observed limits are within the 1 σ uncertainty of the expected limits with a slightly higher central value due to the downward fluctuation in R4.

8 Summary

We have developed an analysis to search for supersymmetry in the final state with a single lepton, b-tagged jets, and large missing transverse momentum. The search focuses on final states resulting from gluino pair production, with $\tilde{g} \to t\bar{t}\tilde{\chi}_1^0$, and hence focuses on high jet multiplicities.

The objects and associated requirements used in the analysis are described in Section 3 and summarized in Table 1. Leptons are required to have $p_T > 20$ GeV and to satisfy an isolation requirement based on the mini-isolation variable. Jets are used down to a p_T threshold of 30 GeV. A novel feature of the analysis is the use of the variable M_J, the sum of the masses of large-R jets, which are formed by clustering standard AK4 PF jets using a radius parameter $R = 1.2$. Used in conjunction with the variable m_T, the transverse mass of the system consisting of the lepton and the missing transverse momentum vector, M_J provides a powerful background estimation method that is well suited to this high jet multiplicity search.

Details of the trigger requirements and the event selection are given in Section 4. The data sample corresponds to 2.1 fb^{-1} and was collected using a single lepton (electron or muon) trigger with $p_T > 15$ GeV and $H_T > 350$ GeV. The baseline event selection and the yields for SM backgrounds and the signal models are given in Table 2. After the baseline selection is applied, we establish signal and control regions in the M_J-m_T plane and perform ABCD calculations to determine the SM background. The ABCD regions in this plane are further divided into subregions in E_T^{miss}, N_{jets}, and N_b. These regions are shown in Fig. 4 and Fig. 5.

The background estimation methodology is described in Section 5. The basis for this ABCD approach is the approximate statistical independence of the M_J and m_T variables. This independence is shown, for example, in Figs. 6, 7, 8, and 9. A correction factor κ^{MC} taken from

[1]The χ^2 is calculated for bins with at least 4 events, using the number of such bins as the number of degrees of freedom. One degree of freedom is subtracted to account for the normalization. The total uncertainty is the sum in quadrature of the bin uncertainty for low M_J plus the square root of the value of the low M_J bin.

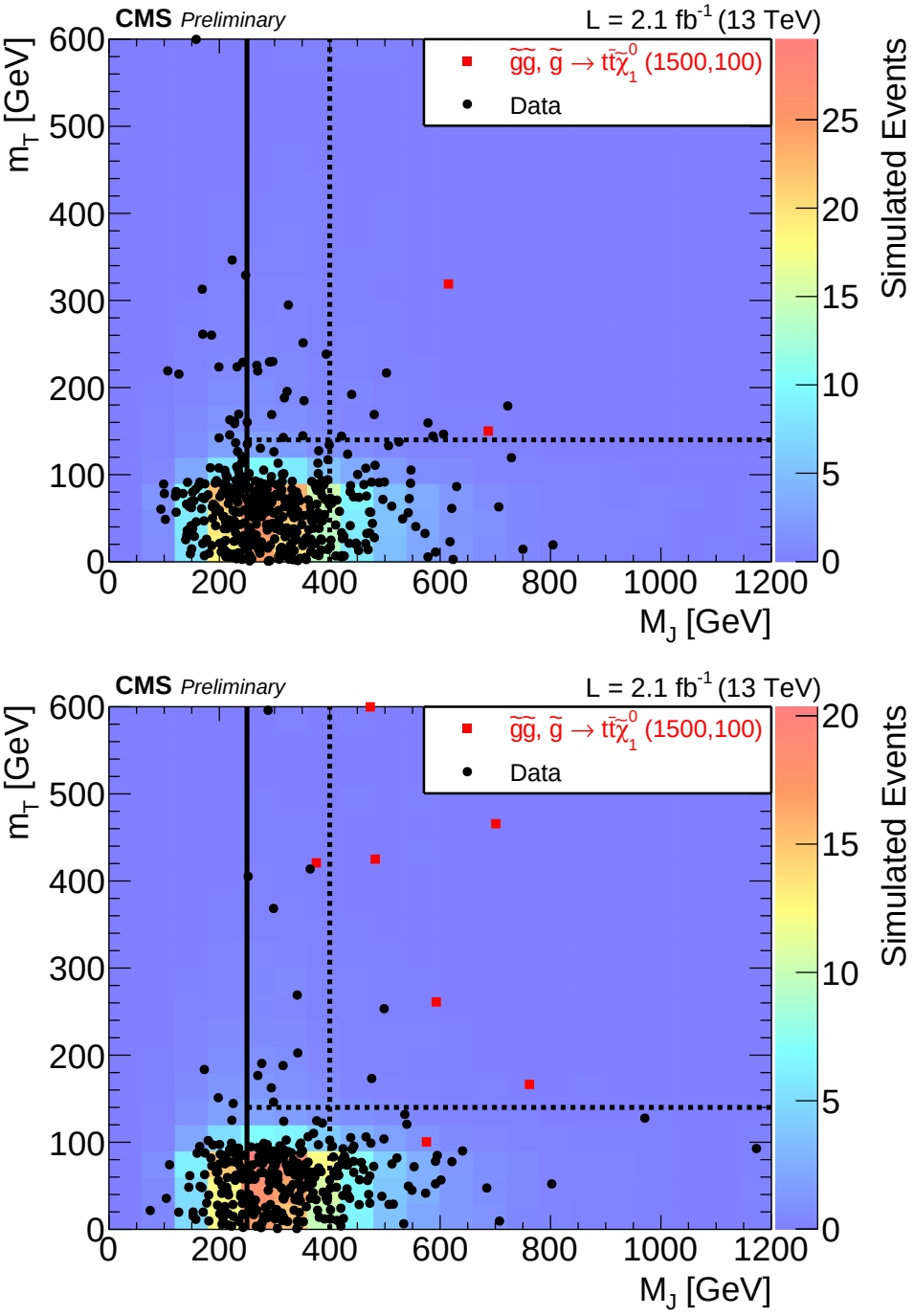

Figure 12: Two-dimensional distributions of m_{T} and M_J with $N_{\mathrm{b}} = 1$ (top) and $N_{\mathrm{b}} \geq 2$ (bottom) after the baseline selection. The colored histogram is all simulated background normalized to the data, the black dots are data, and the red dots are the expected T1tttt(1500,100) yield for 2.1 fb^{-1}.

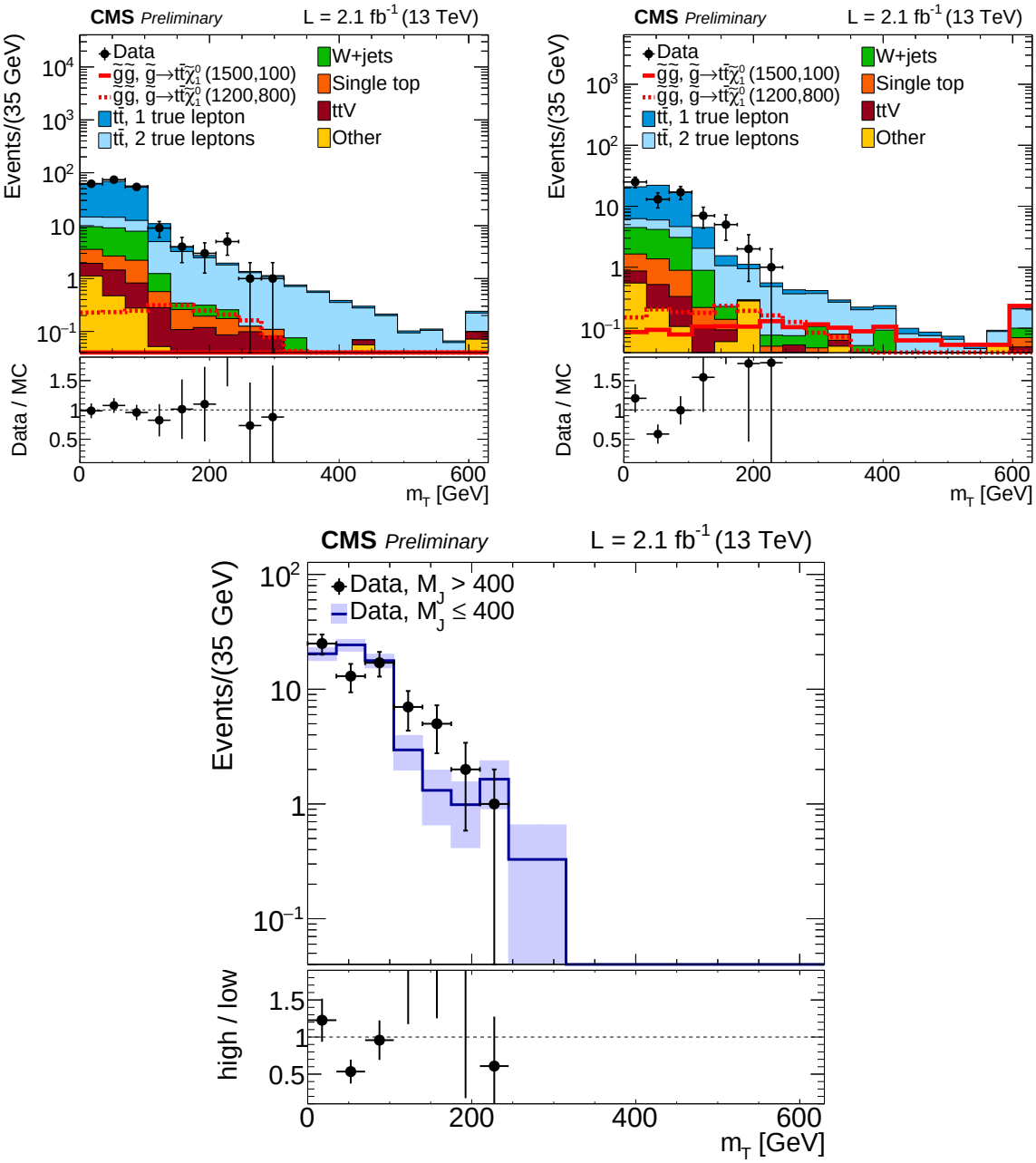

Figure 13: Distributions of m_{T} for events with $N_{\mathrm{b}} = 1$ in data and simulated event samples (MC). Top: m_{T} distributions for $250 < M_J \leq 400\,\mathrm{GeV}$ (left) and $M_J > 400\,\mathrm{GeV}$ (right). The overall MC event yields are normalized to that in the data. Bottom: comparison of the m_{T} distributions for low and high M_J in data, the former normalized to the number of events in the latter. The uncertainties on the ratio plots include the uncertainties from the numerator and denominator added in quadrature.

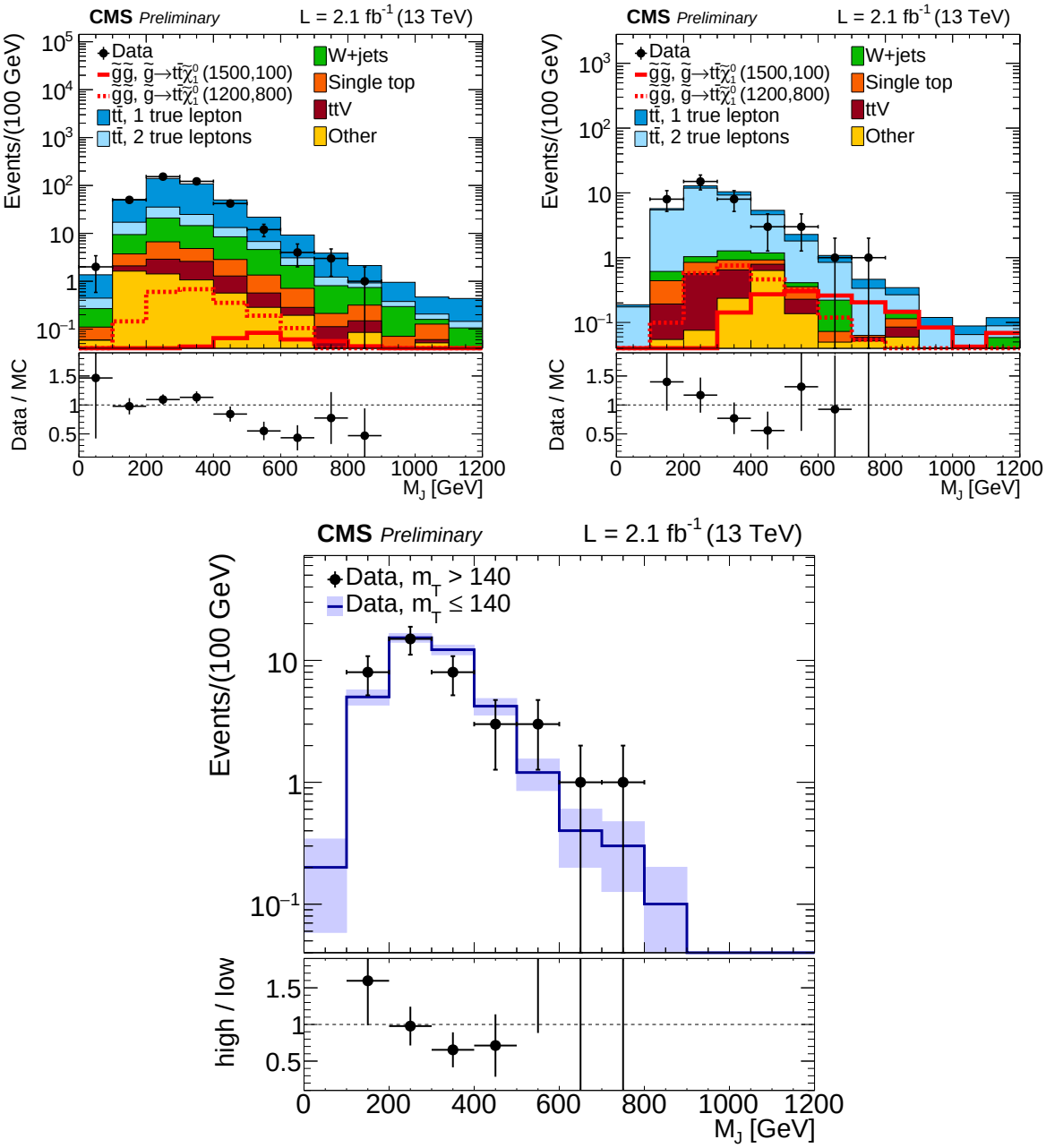

Figure 14: Distributions of M_J for events with $N_b = 1$ in data and simulated event samples (MC). Top: M_J distributions for $m_T \leq 140$ GeV (left) and $m_T > 140$ GeV (right). The overall MC event yields are normalized to that in the data. Bottom: comparison of the M_J distributions for low and high m_T in data, the former normalized to the number of events in the latter. The uncertainties on the ratio plots include the uncertainties from the numerator and denominator added in quadrature.

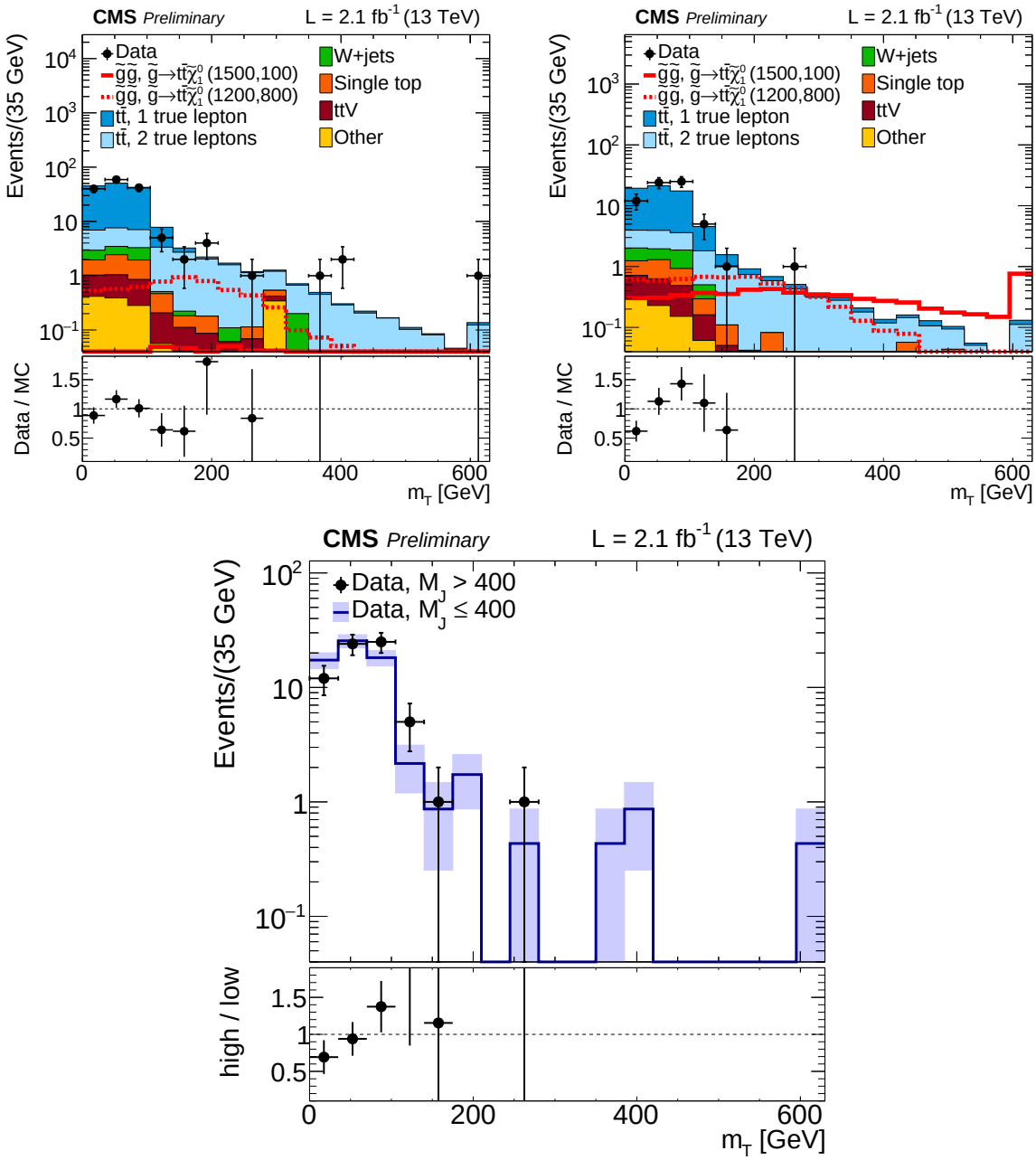

Figure 15: Distributions of m_{T} for events with $N_{\mathrm{b}} \geq 2$ in data and simulated event samples. Top: m_{T} distributions for $250 < M_J \leq 400\,\mathrm{GeV}$ (left) and $M_J > 400\,\mathrm{GeV}$ (right). The overall MC event yields are normalized to that in the data. Bottom: comparison of the m_{T} distributions for low and high M_J in data, the former normalized to the number of events in the latter. The uncertainties on the ratio plots include the uncertainties from the numerator and denominator added in quadrature.

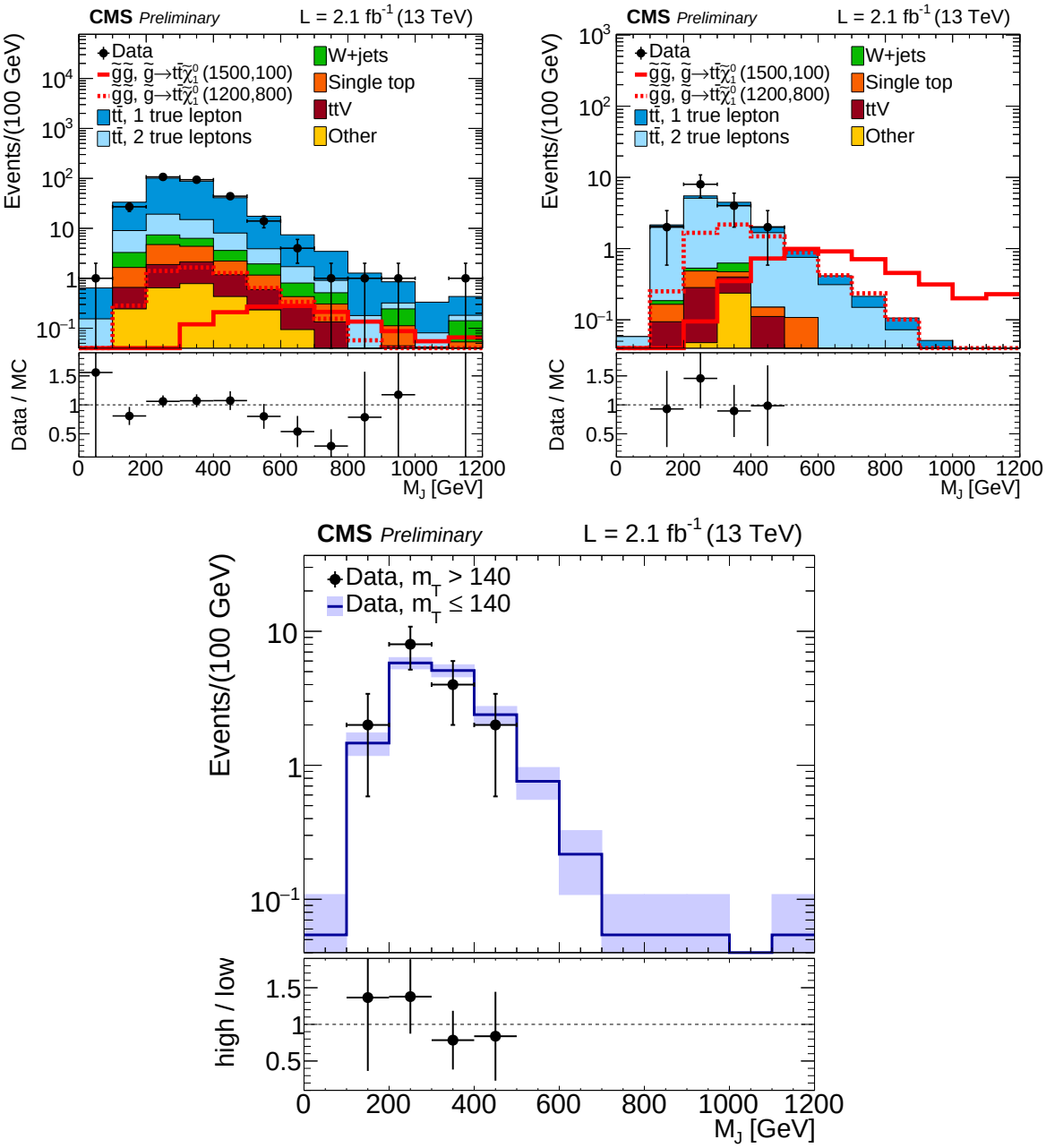

Figure 16: Distributions of M_J for events with $N_b \geq 2$. Top: M_J distributions for $m_T \leq 140\,\text{GeV}$ (left) and $m_T > 140\,\text{GeV}$ (right). The overall MC event yields are normalized to that in the data Bottom: comparison of the M_J distributions for low and high m_T in data, the former normalized to the number of events in the latter. The uncertainties on the ratio plots include the uncertainties from the numerator and denominator added in quadrature.

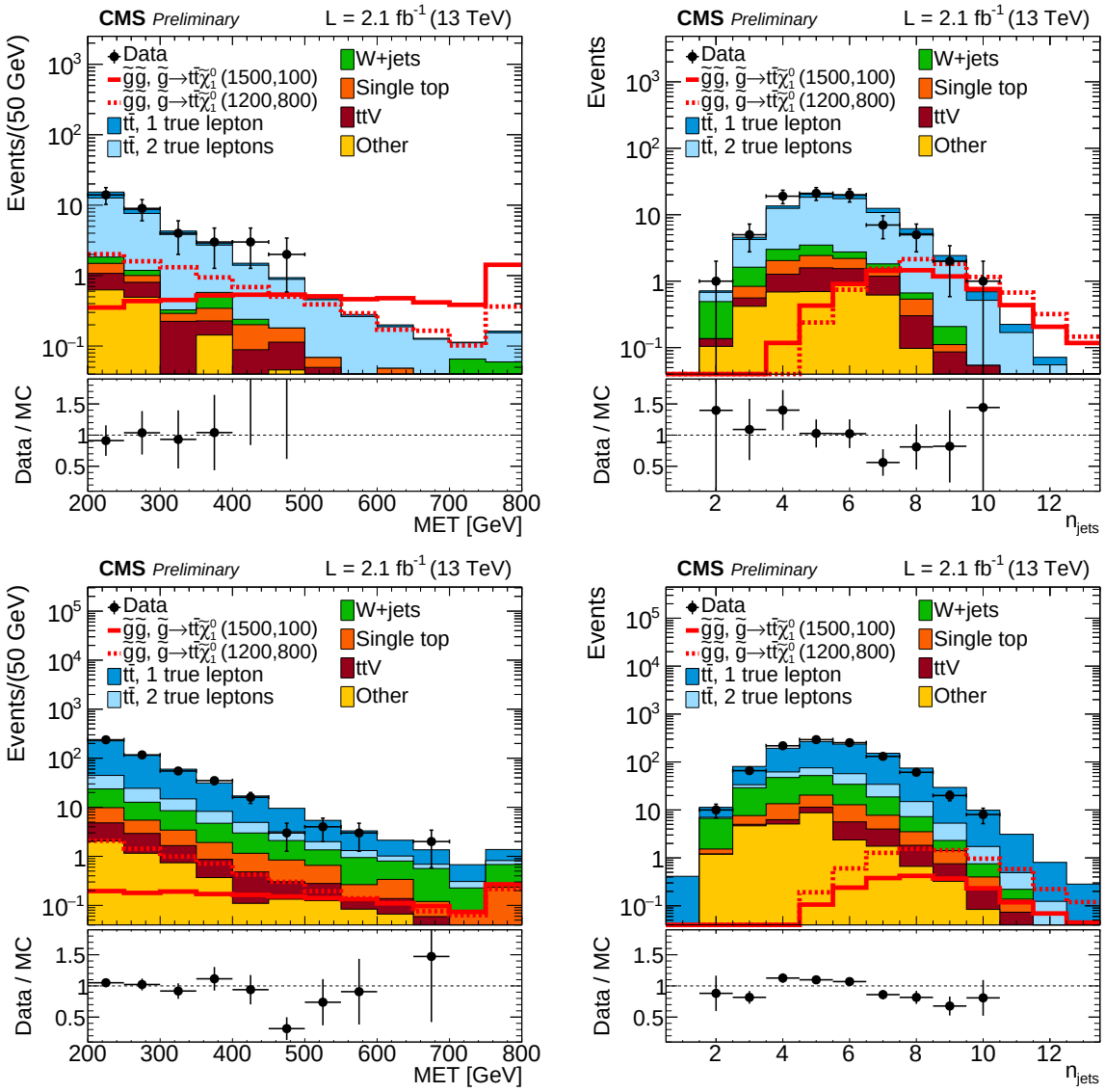

Figure 17: Distributions $E_{\mathrm{T}}^{\mathrm{miss}}$ and N_{jets} for events with $N_{\mathrm{b}} \geq 1$ in data and simulated event samples. Distributions of $E_{\mathrm{T}}^{\mathrm{miss}}$ (left) and N_{jets} (right), for $m_{\mathrm{T}} \leq 140\,\mathrm{GeV}$ (bottom) and $m_{\mathrm{T}} > 140\,\mathrm{GeV}$ (top). The overall MC event yields are normalized to that in the data, with the normalization factor given below the legend.

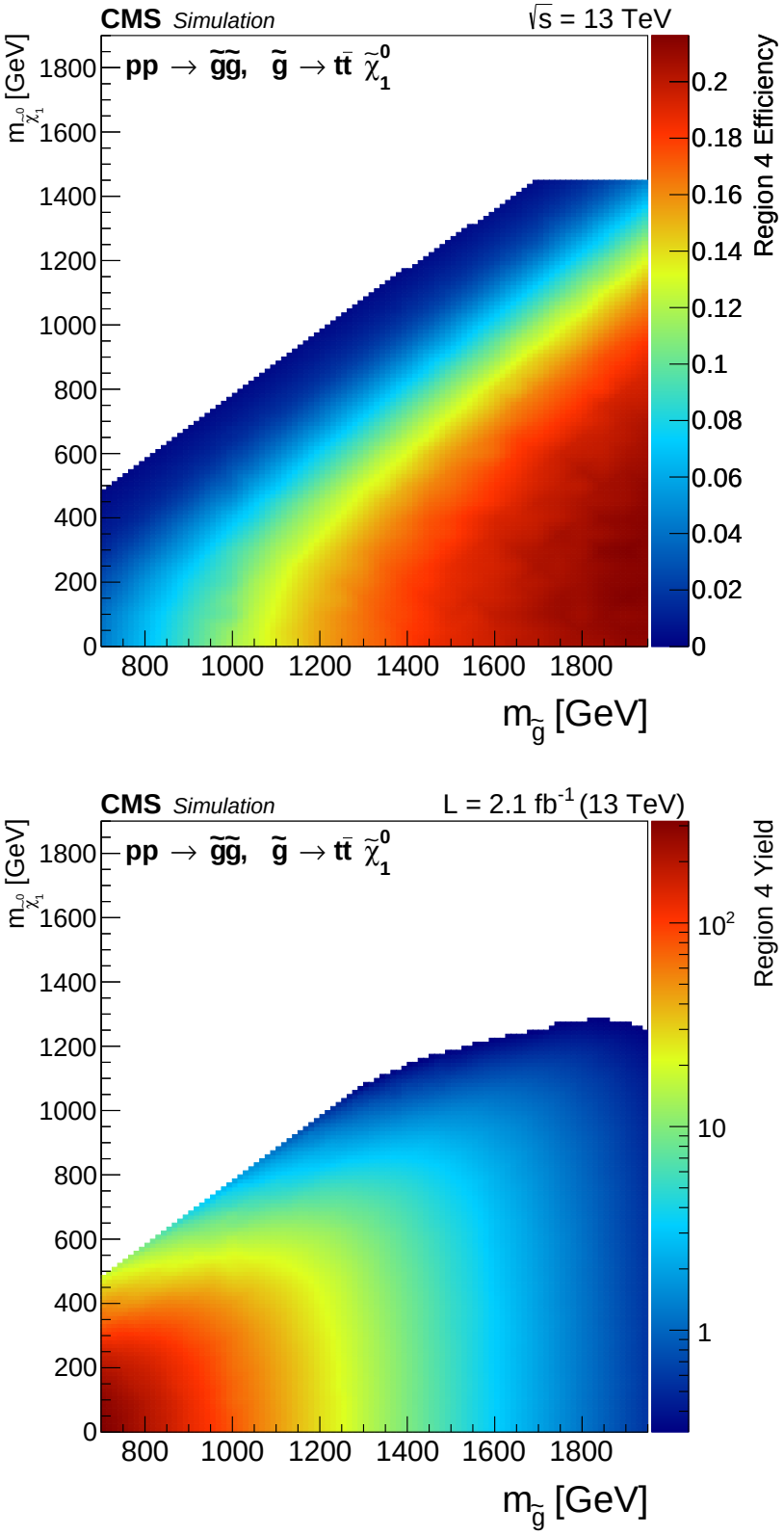

Figure 18: Region 4 signal efficiency (top) and yields normalized to 2.1 fb^{-1} (bottom) in the $m_{\tilde{g}} - m_{\tilde{\chi}_1^0}$ plane.

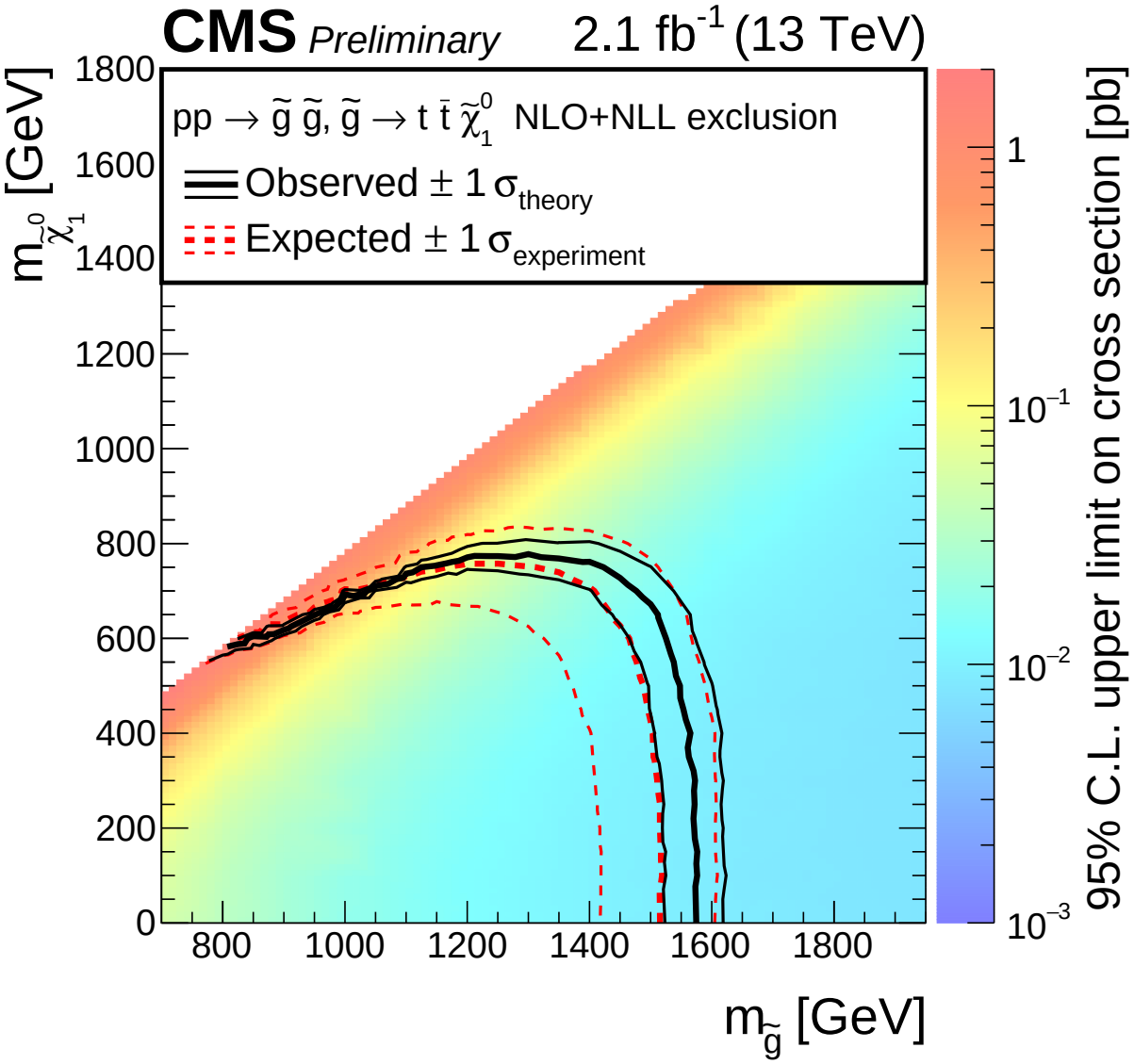

Figure 19: The 95% confidence level upper limits on the production cross section for the pp $\rightarrow$ $\widetilde{g}\widetilde{g}, \widetilde{g} \rightarrow t\bar{t}\tilde{\chi}_1^0$ in the $m_{\widetilde{g}} - m_{\tilde{\chi}_1^0}$ plane.

simulation is used to account for a possible residual correlation between M_J and m_T. Given that the low m_T region is dominated by single-lepton $t\bar{t}$ events, while the high m_T region is dominated by dilepton $t\bar{t}$ events, this absence of a correlation is not obvious. However, simple physics arguments underlie this result. In the signal region with high jet multiplicities, many of the jets orginate from initial-state radiation. This radiation is insensitive to whether the decay of the $t\bar{t}$ system occurs in the single-lepton or dilepton channel.

A binned maximum likelihood fit, discussed in Sec. 5.2, is performed to both determine background estimates and extract the signal yields. To improve the statistical power of the ABCD method, in the low M_J region, the fit integrates over N_{jets} and N_b. The justification for this procedure is that the ratio of yields at high to low values of m_T is only weakly sensitive to these quantities. Both a predictive fit and a global fit are performed. The predictive fit uses only three of the four ABCD regions and provides background estimates for the high-m_T, high-M_J region testing the null hypothesis (no SUSY signal). The global fit uses all four regions and takes into account potential signal contamination in all bins. The exclusion limits are set with the global fit.

The systematic uncertainties on both the background estimation and the signal efficiency are discussed in Section 6. The effects of uncertainties on initial-state radiation, top-quark p_T distributions, $t\bar{t}$ single-lepton contamination at high m_T, and non-$t\bar{t}$ background are estimated with conservative assumptions on the underlying processes. In addition, a powerful test in data using the dilepton sample is performed. The dilepton test provides a robust systematic uncertainty that tests most aspects of the analysis except for contributions from single-lepton $t\bar{t}$ and non-$t\bar{t}$ backgrounds.

Finally, Section 7 presents the results of the predictive and global fits in Table 6. One and two dimensional distributions of the data in the m_T, M_J, E_T^{miss}, and N_{jets} variables are shown in Figs. 12 to 17.

The observed event yields in the signal regions are consistent with the predictions for the SM background contributions, and we set exclusion limits on the gluino pair production cross sections in the $m_{\tilde{g}}$–$m_{\tilde{\chi}_1^0}$ plane. Figure 18 shows the signal efficiency and yields in the high-m_T, high-M_J region, and Fig. 19 presents the cross sections excluded at the 95% confidence level. Gluinos with mass below 1575 GeV are excluded for T1tttt scenarios with low $\tilde{\chi}_1^0$ mass.

References

[1] P. Ramond, "Dual theory for free fermions", *Phys. Rev. D* **3** (1971) 2415, doi:10.1103/PhysRevD.3.2415.

[2] Y. A. Golfand and E. P. Likhtman, "Extension of the algebra of Poincaré group generators and violation of P invariance", *JETP Lett.* **13** (1971) 323.

[3] A. Neveu and J. H. Schwarz, "Factorizable dual model of pions", *Nucl. Phys. B* **31** (1971) 86, doi:10.1016/0550-3213(71)90448-2.

[4] D. V. Volkov and V. P. Akulov, "Possible universal neutrino interaction", *JETP Lett.* **16** (1972) 438.

[5] J. Wess and B. Zumino, "A Lagrangian model invariant under supergauge transformations", *Phys. Lett. B* **49** (1974) 52, doi:10.1016/0370-2693(74)90578-4.

[6] J. Wess and B. Zumino, "Supergauge transformations in four dimensions", *Nucl. Phys. B* **70** (1974) 39, doi:10.1016/0550-3213(74)90355-1.

[7] P. Fayet, "Supergauge invariant extension of the Higgs mechanism and a model for the electron and its neutrino", *Nucl. Phys. B* **90** (1975) 104, doi:10.1016/0550-3213(75)90636-7.

[8] H. P. Nilles, "Supersymmetry, supergravity and particle physics", *Phys. Rep.* **110** (1984) 1, doi:10.1016/0370-1573(84)90008-5.

[9] J. Alwall, P. Schuster, and N. Toro, "Simplified models for a first characterization of new physics at the LHC", *Phys. Rev. D* **79** (2009) 075020, doi:10.1103/PhysRevD.79.075020, arXiv:0810.3921.

[10] J. Alwall, M.-P. Le, M. Lisanti, and J. G. Wacker, "Model-independent jets plus missing energy searches", *Phys. Rev. D* **79** (2009) 015005, doi:10.1103/PhysRevD.79.015005, arXiv:0809.3264.

[11] D. Alves et al., "Simplified models for LHC new physics searches", *J. Phys. G* **39** (2012) 105005, doi:10.1088/0954-3899/39/10/105005, arXiv:1105.2838.

[12] S. Dimopoulos and G. F. Giudice, "Naturalness constraints in supersymmetric theories with nonuniversal soft terms", *Phys. Lett. B* **357** (1995) 573, doi:10.1016/0370-2693(95)00961-J, arXiv:hep-ph/9507282.

[13] R. Barbieri and D. Pappadopulo, "S-particles at their naturalness limits", *JHEP* **10** (2009) 061, doi:10.1088/1126-6708/2009/10/061, arXiv:0906.4546.

[14] M. Papucci, J. T. Ruderman, and A. Weiler, "Natural SUSY endures", *JHEP* **09** (2012) 035, doi:10.1007/JHEP09(2012)035, arXiv:1110.6926.

[15] A. Hook, E. Izaguirre, M. Lisanti, and J. G. Wacker, "High Multiplicity Searches at the LHC Using Jet Masses", *Phys.Rev.* **D85** (2012) 055029, doi:10.1103/PhysRevD.85.055029, arXiv:1202.0558.

[16] T. Cohen, E. Izaguirre, M. Lisanti, and H. K. Lou, "Jet Substructure by Accident", *JHEP* **1303** (2013) 161, doi:10.1007/JHEP03(2013)161, arXiv:1212.1456.

[17] S. El Hedri, A. Hook, M. Jankowiak, and J. G. Wacker, "Learning How to Count: A High Multiplicity Search for the LHC", *JHEP* **1308** (2013) 136, doi:10.1007/JHEP08(2013)136, arXiv:1302.1870.

[18] CMS Collaboration, "Commissioning the performance of key observables used in SUSY searches with the first 13 TeV data", DP 2015-035, CMS, 2015.

[19] J. Alwall et al., "The automated computation of tree-level and next-to-leading order differential cross sections, and their matching to parton shower simulations", *JHEP* **07** (2014) 079, doi:10.1007/JHEP07(2014)079, arXiv:1405.0301.

[20] S. Alioli, P. Nason, C. Oleari, and E. Re, "NLO single-top production matched with shower in POWHEG: s- and t-channel contributions", *JHEP* **09** (2009) 111, doi:10.1007/JHEP02(2010)011, 10.1088/1126-6708/2009/09/111, arXiv:0907.4076. [Erratum: JHEP02,011(2010)].

[21] E. Re, "Single-top Wt-channel production matched with parton showers using the POWHEG method", *Eur. Phys. J.* **C71** (2011) 1547, doi:10.1140/epjc/s10052-011-1547-z, arXiv:1009.2450.

[22] NNPDF Collaboration, "Parton distributions for the LHC Run II", *JHEP* **04** (2015) 040, doi:10.1007/JHEP04(2015)040, arXiv:1410.8849.

[23] T. Sjöstrand, S. Mrenna, and P. Z. Skands, "A brief introduction to PYTHIA 8.1", *Comput. Phys. Commun.* **178** (2008) 852, doi:10.1016/j.cpc.2008.01.036, arXiv:0710.3820.

[24] GEANT4 Collaboration, "GEANT4—a simulation toolkit", *Nucl. Instrum. Meth. A* **506** (2003) 250, doi:10.1016/S0168-9002(03)01368-8.

[25] A. Giammanco, "The Fast Simulation of the CMS Experiment", *Journal of Physics: Conference Series* **513** (2014), no. 2, 022012.

[26] M. Czakon, P. Fiedler, and A. Mitov, "The total top quark pair production cross-section at $\mathcal{O}(\alpha_S^4)$", *Phys. Rev. Lett.* **110** (2013) 252004, doi:10.1103/PhysRevLett.110.252004, arXiv:1303.6254.

[27] W. Beenakker, R. Hopker, M. Spira, and P. M. Zerwas, "Squark and gluino production at hadron colliders", *Nucl. Phys.* **B492** (1997) 51–103, doi:10.1016/S0550-3213(97)00084-9, arXiv:hep-ph/9610490.

[28] A. Kulesza and L. Motyka, "Threshold resummation for squark-antisquark and gluino-pair production at the LHC", *Phys. Rev. Lett.* **102** (2009) 111802, doi:10.1103/PhysRevLett.102.111802, arXiv:0807.2405.

[29] A. Kulesza and L. Motyka, "Soft gluon resummation for the production of gluino-gluino and squark-antisquark pairs at the LHC", *Phys. Rev. D* **80** (2009) 095004, doi:10.1103/PhysRevD.80.095004, arXiv:0905.4749.

[30] W. Beenakker et al., "Soft-gluon resummation for squark and gluino hadroproduction", *JHEP* **12** (2009) 041, doi:10.1088/1126-6708/2009/12/041, arXiv:0909.4418.

[31] M. Cacciari, G. P. Salam, and G. Soyez, "The anti-kt jet clustering algorithm", *JHEP* **0804:063** (2008) doi:10.1088/1126-6708/2008/04/063.

[32] CMS Collaboration, "Particle flow event reconstruction in CMS and performance for jets, taus and $E_{\mathrm{T}}^{\mathrm{miss}}$", CMS Physics Analysis Summary CMS-PAS-PFT-09-001, CERN, 2009.

[33] CMS Collaboration, "Commissioning of the particle-flow event reconstruction with the first LHC collisions recorded in the CMS detector", CMS Physics Analysis Summary CMS-PAS-PFT-10-001, CERN, 2010.

[34] CMS Collaboration, "Performance of electron reconstruction and selection with the CMS detector in proton-proton collisions at s = 8 TeV", *JINST* **10** (2015), no. 06, P06005, doi:10.1088/1748-0221/10/06/P06005, arXiv:1502.02701.

[35] CMS Collaboration, "Performance of CMS muon reconstruction in pp collision events at $\sqrt{s} = 7$ TeV", *JINST* **7** (2012) P10002, doi:10.1088/1748-0221/7/10/P10002, arXiv:1206.4071.

[36] K. Rehermann and B. Tweedie, "Efficient Identification of Boosted Semileptonic Top Quarks at the LHC", *JHEP* **03** (2011) 059, doi:10.1007/JHEP03(2011)059, arXiv:1007.2221.

[37] CMS Collaboration, "Determination of jet energy calibration and transverse momentum resolution in CMS", *JINST* **06** (2011) P11002, doi:10.1088/1748-0221/6/11/P11002, arXiv:1107.4277.

[38] M. Cacciari and G. P. Salam, "Pileup subtraction using jet areas", *Phys. Lett. B* **659** (2008) 119, doi:10.1016/j.physletb.2007.09.077, arXiv:0707.1378.

[39] CMS Collaboration, "Determination of jet energy calibration and transverse momentum resolution in CMS", *JINST* **6** (2011) P11002, doi:10.1088/1748-0221/6/11/P11002, arXiv:1107.4277.

[40] CMS Collaboration, "Jet Performance in pp Collisions at $\sqrt{s}$=7 TeV", CMS Physics Analysis Summary CMS-PAS-JME-10-003, 2010.

[41] CMS Collaboration, "Identification of b-quark jets with the CMS experiment", *JINST* **8** (2013) P04013, doi:10.1088/1748-0221/8/04/P04013, arXiv:1211.4462.

[42] CMS Collaboration, "Performance of b tagging at $\sqrt{s} = 8$ TeV in multijet, $\mathrm{t\bar{t}}$ and boosted topology events", CMS Physics Analysis Summary CMS-PAS-BTV-13-001, CERN, 2013.

[43] CMS Top PAG, "p_{T} (top-quark) based reweighting of ttbar MC", (2014). https://twiki.cern.ch/twiki/bin/viewauth/CMS/TopPtReweighting.

[44] CMS Collaboration, "Search for top-squark pair production in the single-lepton final state in pp collisions at $\sqrt{s}$ = 8 TeV", *Eur. Phys. J.* **C73** (2013), no. 12, 2677, doi:10.1140/epjc/s10052-013-2677-2, arXiv:1308.1586.